Observable consequences of self-irradiation damage in a MIMAS-type MOX nuclear fuel as analyzed by x-ray diffraction, electron microprobe analysis, and Raman imaging. A possible methodological approach

Orhun Kahraman, Florent Lebreton, Philippe Martin, Michel Mermoux

▶ **To cite this version:**

Orhun Kahraman, Florent Lebreton, Philippe Martin, Michel Mermoux. Observable consequences of self-irradiation damage in a MIMAS-type MOX nuclear fuel as analyzed by x-ray diffraction, electron microprobe analysis, and Raman imaging. A possible methodological approach. Journal of Applied Physics, 2022, 132 (11), pp.115106. 10.1063/5.0103348 . hal-04305414

HAL Id: hal-04305414
https://hal.science/hal-04305414

Submitted on 24 Nov 2023

HAL is a multi-disciplinary open access archive for the deposit and dissemination of scientific research documents, whether they are published or not. The documents may come from teaching and research institutions in France or abroad, or from public or private research centers.

L'archive ouverte pluridisciplinaire **HAL**, est destinée au dépôt et à la diffusion de documents scientifiques de niveau recherche, publiés ou non, émanant des établissements d'enseignement et de recherche français ou étrangers, des laboratoires publics ou privés.

ACCEPTED MANUSCRIPT

Journal of Applied Physics

AIP Publishing

This is the author's peer reviewed, accepted manuscript. However, the online version of record will be different from this version once it has been copyedited and typeset.
PLEASE CITE THIS ARTICLE AS DOI: 10.1063/5.0103348

Observable consequences of self-radiation damage in a MIMAS-type MOX nuclear fuel as analyzed by x-ray diffraction, electron microprobe analysis and Raman imaging. A possible methodological approach.

Orhun Kahraman,[1,2] Florent Lebreton[1], Philippe Martin[1], Michel Mermoux[2]

[1]CEA, DES, ISEC, DMRC, Univ. Montpellier, Marcoule, France

[2] Univ. Grenoble Alpes, Univ. Savoie Mont Blanc, CNRS, Grenoble INP, LEPMI, 38000 Grenoble, France

Corresponding author: philippe-m.martin@cea.fr

ABSTRACT

One of the challenges of Pu multi-recycling, to be used to produce MOx fuel, lies in its isotopic composition. Further recycling enriches the isotopy towards ^{238}Pu, ^{240}Pu and ^{241}Pu, which have much higher specific activities than the ^{239}Pu isotope, meaning that those fuels are subjected to strong self-irradiation, provoking defect accumulation in the $(U,Pu)O_2$ crystal lattice. A combination of three different techniques, XRD, EPMA and RS (X-Ray diffraction, Electron Probe Micro-analysis and Raman spectroscopy respectively) was implemented to characterize a particular self-irradiated, ^{238}Pu, ^{240}Pu and ^{241}Pu-enriched MIMAS-type MOx fuel sample, which had been stored for 15 years at room temperature under an inert atmosphere, to maximize irradiation effects. For comparison purposes, a specimen from the same batch was submitted to a thermal treatment and was completely analyzed in the two months following this treatment. Two of these methods (EPMA and RS) were used in their imaging mode. In particular, four spectral characteristics could be extracted from the Raman spectra. However, because of the inherent heterogeneity to this particular MOx material, the results had to be analyzed in part in a rather statistical way. This combination of techniques first allowed determining the local Pu content. Then, the effects of self-irradiation were analyzed in terms of lattice parameter swelling, defect injection, and resonant scattering. The merits and uncertainties associated with these methods are discussed in terms of macro and/or micro strain. Finally, the Raman spectroscopy of $(U,Pu)O_2$, in the 0-40% range, was revisited in part, in an indirect way however.

ACCEPTED MANUSCRIPT
Journal of Applied Physics
AIP Publishing
This is the author's peer reviewed, accepted manuscript. However, the online version of record will be different from this version once it has been copyedited and typeset.
PLEASE CITE THIS ARTICLE AS DOI: 10.1063/5.0103348

1. INTRODUCTION

For more than 30 years, France has implemented industrially the spent UO_2 nuclear fuel reprocessing. It indeed increases the amount of fissile material that can be obtained from extracted natural uranium (U), as well as largely decreases the volume and ecological footprint of the final waste. The recovered plutonium (Pu), mainly composed of fissile ^{239}Pu, is used to produce $(U,Pu)O_2$ MOx (Mixed Oxides fuel) with a Pu content ranging between 6 and 9 % Pu/(U+Pu) optimized for the current Pressurized Water Reactor (PWR) fleet. Nevertheless, the accomplishment of a fully closed fuel cycle relies on the multi-recycling of Pu, *i.e.* the continuous extraction of Pu from the spent MOx fuel [1].

MOX fuels are dense ceramic pellets (95% of the theoretical density). From a crystallographic point of view, these materials present the same fluorite-type structure (Fm-3m, space group n°225) over the whole Pu/(U+Pu) range from UO_2 to PuO_2. The cations form a face centered cubic sublattice in which the oxygen occupy the tetrahedral positions. This structure can accommodate the full range of Pu content of any isotopy and is thus used for current MOX fuels and will be used for future MOX fuels after Pu multi-recycling.

One of the challenges of Pu multi-recycling lies in its isotopic composition as a further recycling enriches the isotopy towards ^{238}Pu, ^{240}Pu and ^{241}Pu at the cost of the ^{239}Pu isotope. Due to the high alpha (α) activities of ^{238}Pu (633.4 GBq/g), ^{240}Pu (8.4 GBq/g) and ^{241}Am (produced by beta (β) decay of ^{241}Pu, 127 GBq/g) compared to that of ^{239}Pu (2.3 GBq/g), these new fuels are subjected to strong and spontaneous alpha self-irradiation.

Upon α self-irradiation, the recoil nucleus is emitted with an energy around 100 keV. According to the Stopping and Range of Ions in Matter (SRIM) code [2], about 1300 lattice atoms are displaced in a few tens of nm from its initial position [3]. Even if a large amount of point defects is generated in a small volume, a significant part is annihilated through recombination. An α particle (He nucleus) is also emitted with an energy of about 5.5 MeV. Still according to the SRIM code, it generates about 200 atomic displacements and the associated point defects are located mostly in the end of its ≈10 µm-long path. Additionally, the resulting helium atoms accumulate in the structure as interstitials, inside vacancy clusters or even initial pores. Such a process provokes defect accumulation in the fuel crystal lattice, resulting in a progressive alteration of its physico-chemical properties and microstructure [4,5]. Thus, it becomes necessary to consider self-irradiation consequences during the storage of the fuel between manufacturing and its subsequent use in reactor.

Self-irradiation consequences have been studied for several years for most of actinide oxides (AnO_2) and some of their mixed oxides [6–10]. From a structural point of view, at a macroscopic scale, an immediate consequence is the progressive AnO_2 lattice swelling induced by the damage cascades caused by both recoil nuclei, He ions and/or the accumulation of He atoms over time. The lattice parameter increase due to the α-decay of Pu isotopes and its evolution

ACCEPTED MANUSCRIPT
Journal of Applied Physics
AIP Publishing
This is the author's peer reviewed, accepted manuscript. However, the online version of record will be different from this version once it has been copyedited and typeset.
PLEASE CITE THIS ARTICLE AS DOI: 10.1063/5.0103348

vs time are rather well documented [11–13]. As a matter of fact, one generally observes that the swelling first increases rapidly and then reaches a saturation value, close to 0.3% for the MOx materials. The time needed to reach saturation corresponds to a given cumulated α dose and thus depends on the α dose rate, thus on the local material and isotopic composition.

Several authors have investigated the lattice parameter increase vs time using various samples such as UO_2 doped with ^{238}Pu, $^{238}PuO_2$, $^{239}PuO_2$, $^{241}AmO_2$ and $^{243}CmO_2$ and some of their mixed oxides [6–14]. The saturation phenomenon was first analyzed by W.J. Weber [15–17] who suggested a steady state between defect formation and their self-healing. For each single isotope, a same empirical relationship was reported, correlating the lattice parameter increase to the storage time according to:

$$\Delta a/a_0 = A[1 - e^{(-B \cdot \lambda \cdot t)}] \quad (1)$$

Where a_0 (Å) is defect free lattice parameter, Δa is the increase of lattice parameter caused by self-irradiation, λ (s^{-1}) is the time decay constant of the alpha-decaying isotope, t (s) the self-irradiation time, A (dimensionless) the maximum relative swelling and B (dimensionless) a swelling kinetic constant. Here, a_0, λ, A and B are element- and isotopic composition-dependent constants. A and B parameters are usually determined by fitting the experimental lattice swelling data to Eq. 1[11].

Because MOx fuels contain more than one single Pu isotope, an effective decay constant λ' has to be considered [11]:

$$\lambda' = C_{Pu} \sum \lambda_i C_i \quad (2)$$

where C_{Pu} is the Pu/(Pu+^{241}Am) content, λ_i the decay constant of each Pu (or ^{241}Am) isotope and C_i the Pu isotopic composition. Five different Pu isotopes and one Am isotope are to be considered here: ^{238}Pu, ^{239}Pu, ^{240}Pu, ^{241}Pu, ^{242}Pu and ^{241}Am.

It is worth mentioning that the α decay of an actinide atom is also responsible for a change in the composition, from Pu to U or Am to Np. In most actinide dioxide, there is an almost linear correlation between the average cationic ionic radius and the lattice parameter. As the daughter isotope usually presents a different ionic radius than its parent, the decay results in a change of the lattice parameter. The latter is however not significant compared to the lattice parameter swelling described in the previous paragraph and it is thus generally not taken into account.

Even though the lattice parameter swelling is well described in the literature, the associated mechanisms at a more microscopic scale are not fully understood. The identification and the description of the point or extended defects, their stability vs time and temperature, and the

ACCEPTED MANUSCRIPT
Journal of Applied Physics
AIP Publishing
This is the author's peer reviewed, accepted manuscript. However, the online version of record will be different from this version once it has been copyedited and typeset.
PLEASE CITE THIS ARTICLE AS DOI: 10.1063/5.0103348

subsequent consequences on the evolution of the lattice parameter are yet to be revealed and described.

At such an atomistic length scale, irradiation events mainly lead to electronic excitation but also to the creation of point defects such as vacancies or interstitials, as well as other extended defects. The presence of these defects, and their time evolution, can be visualized using transmission electron microscopy (TEM), see for example Refs.[3,13]. The creation of these defects and their evolution over time can also be studied by molecular dynamics simulations[18,19]. Even if the doses and time scales used in these simulations do not necessarily correspond to those characteristic of self-irradiation effects, they most probably allow to propose a first scenario in which point defects (Frenkel pairs, but more generally vacancies and interstitials) first accumulate in the material and then progressively aggregate to form interstitials clusters, voids, Frank loops, and then perfect dislocations. After a given cumulated dose, a steady state is reached and dislocations reorganize into forests of dislocations, creating misoriented nanodomains [18,19]. Basically, the microstructure change induced by this scenario seems consistent with the main TEM observations [3,13]. Thus, the evolution from point defects toward extended defects contributes to minimize the overall elastic strain in the samples, explaining in part the saturation of the lattice parameter increase.

Finally, it is widely documented that the damage accumulated through α (internal or external) irradiation can be recovered through thermal annealing for temperatures higher than 1473 K [11,15,20]. In all cases, it was observed that defect healing was achieved in three different stages, which most probably correspond to the recovery of at least three different types of defects, with increasing activation energies.

The purpose of the present paper is in part to analyze this phenomenon for a particular MOx fuel, notably enriched with ^{238}Pu and ^{241}Am. A small fraction of ^{241}Am is indeed accumulated in the fuel due to ^{241}Pu fast β decay. As we will see in what follows, this phenomenon could not be studied continuously vs time, this work is ongoing. Therefore, the MOx material status after 15 years of storage, which ensured that saturation of the swelling is completely reached, and the one after annealing at high temperature, in order to recover a material assumed to be defect-free, will be compared. The selected MOx material was a MIMAS-type (MIcronized - MASter blend) one.

As we will see more in details below, this material is highly heterogeneous, composed of agglomerates whose sizes are in the 10 - 30 µm range. Due to the highly heterogeneous nature of this particular MOx material, spatially resolved techniques of structural analysis are to be privileged, in addition to X-ray diffraction (XRD) which gives access to the different lattice parameters. One must keep in mind that those lattice parameters values are representing "mean" values. As a matter of fact, the coupling of these methods should allow to track the local Pu content, the oxygen stoichiometry, the expansion of the lattice parameter, as well as

ACCEPTED MANUSCRIPT
Journal of Applied Physics
AIP Publishing
This is the author's peer reviewed, accepted manuscript. However, the online version of record will be different from this version once it has been copyedited and typeset.
PLEASE CITE THIS ARTICLE AS DOI: 10.1063/5.0103348

the presence of structural defects induced by self-irradiation. Electron-based techniques, such as Electron Probe Micro Analysis (EPMA), give access to the local Pu content, at the µm scale. Furthermore, Raman spectroscopy (RS), which can be operated down to the sub-micron scale, effectively appears as another candidate. RS can effectively be operated in mapping or imaging modes, giving access to the spatial distribution of each compound. With the development of remote Raman microscopic facilities allowing analysis in shielded areas, this technique effectively allows the analysis of actinide oxides, see for example [21–25] and references herein. A literature survey shows that this method is sensitive to some deviations from the perfect fluorite structure (in particular lattice expansion, defects, O stoichiometry), even if some interpretations are still subject to debate, see again Refs [22,26] and references herein.

Thus, in the present study, this combination of techniques (XRD, EPMA and RS) was used to track and analyze the effects of self-irradiation on this specific MIMAS-type fuel, with some emphasis on the use of Raman imaging. Of course, the use of this combination of techniques for the understanding of irradiation effects in its broadest sense is not new. By contrast, works using EPMA and RS in their imaging modes are scarcer, to our knowledge. EPMA and RS allow sample imaging, giving among other parameters Pu composition maps. Both methods provide a large amount of data. This should not be seen as a handicap here since they can be discussed in a more or less statistical way.

The results (local Pu content in particular) will first be analyzed using rather strong assumptions. In particular, the annealed MOx material is considered to be stoichiometric and strain-free for simplification and most importantly for comparison purposes. Then, the data sets obtained for the two samples are compared. Finally, and more generally, the characteristics extracted from the Raman spectra will be discussed in terms of size, strain, structural defects incorporation, and resonant scattering.

2. EXPERIMENTAL

A. MOx material

The selected MOx material was a MIMAS-type (MIcronized - MASter blend) one. Briefly, this fuel is produced by a two-step process consisting of blending and milling of UO_2 and PuO_2 powders (master mix), followed by dilution with UO_2 to the targeted U/Pu ratio. During the sintering (1700°C-4h), the close contact between the micronized UO_2 and PuO_2 particles induces a partial interdiffusion and therefore the formation of a $(U,Pu)O_2$ solid solution with varying Pu contents, depending on their location in the material[27]. Such a fabrication process leads to a sintered ceramic material consisting in three distinct "phases":

- U-rich agglomerates resulting from UO_2 used for dilution,
- Pu-rich agglomerates resulting from the master mix and thus presenting a Pu/(U+Pu) content around 30 wt.%,

ACCEPTED MANUSCRIPT
Journal of Applied Physics
AIP Publishing
This is the author's peer reviewed, accepted manuscript. However, the online version of record will be different from this version once it has been copyedited and typeset.
PLEASE CITE THIS ARTICLE AS DOI: 10.1063/5.0103348

- a "matrix" with intermediate Pu contents ranging between those of the two other agglomerates. The "matrix" is also known as the so-called "coating phase"[22,23,28], this denomination is used hereafter.

The starting material (from now on referred as "aged sample") was taken from a batch synthesized in 2007. In 2007, this particular material had a mean Pu+Am/(U+Pu+^{241}Am) content of about 10% in mass together with an ^{241}Am/(Pu+^{241}Am) fraction of 1.48% in mass. As its spatial distribution in the samples is extremely heterogeneous, the overall Pu content was not precisely investigated in this study. Only the local composition was precisely determined. We note in passing that the Pu/(U+Pu+^{241}Am) content will be evaluated by using EPMA, XRD and RS. The last two methods give rather atomic ratios (at%.), while EPMA yields mass values (wt%). However, because of the small difference in average mass between U and Pu isotopes, we will no longer make a clear distinction between wt% and at% as the difference between these two values is below the uncertainties of the extracted quantities.

Since 2007, the MOx pellets were stored at room temperature in inert (N_2) atmosphere. The initial and present isotopic composition are summarized in Table 1, together with their corresponding half-life's and decay constants.

From Table 1, the main information is probably the enrichment in Am, close to a factor of five, upon self-irradiation. The spatial distribution of this element in the sample has to follow that of Pu. It is thus expected that the main consequences of this Am enrichment are to be found in the Pu rich clusters. We will discuss them briefly in the last part of this paper.

Table 1 *Initial (date of manufacture) and final (date of this study) isotopic composition (Isotope/(Pu + Am) or isotope/U) of MIMAS MOX fuel considered in this work, and their corresponding half-life and decay constants (all values correspond to α decays, except for ^{241}Pu where it is disambiguated).*

Isotope	Half-life (year)	Specific activity (GBq/g)	Decay constant (s^{-1})	Isotopic Fraction (wt %) in 2007	Isotopic Fraction (wt %) in 2022
^{238}Pu	8.77×10^{1}	633.4	2.505×10^{-10}	2.41	2.1
^{239}Pu	2.41×10^{4}	2.3	9.116×10^{-13}	53.9	54.1
^{240}Pu	6.56×10^{3}	8.4	3.349×10^{-12}	25.8	25.8
^{241}Pu	3.20×10^{5} 1.43×10^{1}	0.2 3830.4	6.869×10^{-14} 1.533×10^{-9}	8.91	4.29
^{241}Am	4.321×10^{2}	127.0	5.086×10^{-11}	1.48	6.14
^{242}Pu	3.73×10^{5}	0.1	5.888×10^{-14}	7.50	7.53
^{235}U	7.04×10^{8}	8.0×10^{-5}	3.120×10^{-17}	0.30	0.30
^{238}U	4.47×10^{9}	1.24×10^{-5}	4.916×10^{-18}	99.74	99.74

From Eq. 2, knowing A and B parameters (2.9×10^{-3} and -12 000, respectively[9]), it is possible to estimate the times to reach the saturation in the lattice parameter increase of the three

ACCEPTED MANUSCRIPT
Journal of Applied Physics
AIP Publishing
This is the author's peer reviewed, accepted manuscript. However, the online version of record will be different from this version once it has been copyedited and typeset.
PLEASE CITE THIS ARTICLE AS DOI: 10.1063/5.0103348

phases in the MIMAS sample. As a general observation, the saturation is indeed reached after a cumulated dose of about $8.0x10^{17}$ $\alpha.g^{-1}$, as it was investigated by Horlait et al.[12] for the self-irradiation effect in $(U,Am)O_2$ samples. This dose corresponds to an approximate damage level of 0.20 dpa. According to these assumptions, the times required for saturation of the three phases can be estimated, see Table 2. Computing the values given in Table 2, it is implicitly considered that the self-irradiation effects are confined in the different phases, which is obviously a crude approximation. Nevertheless, it is possible to estimate the time required for the swelling saturation.

Table 2 *Approximate durations to reach saturation for the U-rich, Pu rich and coating phases.*

	Average Pu/(U+Pu) content	Time needed to reach 0.3% swelling (years)
U-rich agglomerates	3% (Assumed)	34.4
Coating phase	10%	10.3
Pu-rich agglomerates	30%	3.4

For the present EPMA and RS investigation, aged MOx pellets were cut to get different specimens. All these specimens were subsequently polished up to the mirror state on one side to get metallographic cuts. One of those specimens (from now on referred as "annealed sample") was submitted to a thermal treatment. The annealing conditions, 8 hours at 1473 K under an atmosphere composed of Ar/4.3 $\%H_2$/1200ppm H_2O, ($\Delta G_{O2} \approx$ -420 kJ/mol at 1473K) ensured to keep the oxygen to metal (O/M) ratio as close as possible to 2.00. Cooling of the sample down to room temperature (RT) was performed at 6°C/min, under the same atmosphere. The Am enrichment is also reflected in the annealed sample, meaning that both annealed and aged samples should have a quite similar Am content. The annealed sample is thus not fully representative of the as fabricated material, but it can be considered as a "defect-free" replica of the aged, self-irradiated sample. The full structural analysis of this sample has been performed within less than two months after annealing. In particular, Raman and XRD data have been obtained one month and two days after the annealing, respectively. During that period, Eq. 2 shows that less than ≈ 10 % of the saturation value may develop in the Pu-rich agglomerates.

Both samples were then stored in gloveboxes in inert atmosphere (N_2) to prevent surface oxidation.

B. XRD

The XRD samples were prepared by crushing and mixing in an agate mortar 150-200 milligrams of MOx with ~20 mg of Au. Au was used as an internal reference for 2θ position (Sigma-Aldrich, purity >99.9%) and an organic grease to glue the powder to the plate (Bruker Si low background sample holder) as detailed in Vauchy et al [29].

XRD was performed using a Bruker D8 Advance diffractometer in θ−θ Bragg−Brentano geometry. It was equipped with a copper source [$\lambda(K_{\alpha1}/_{\alpha2})$ = 1.540598/1.54443 Å] and a Bruker

ACCEPTED MANUSCRIPT
Journal of Applied Physics
AIP Publishing
This is the author's peer reviewed, accepted manuscript. However, the online version of record will be different from this version once it has been copyedited and typeset.
PLEASE CITE THIS ARTICLE AS DOI: 10.1063/5.0103348

LYNXEYE linear detector with a 3° opening angle. Diffraction patterns were recorded from 2θ = 20 to 120°, with a 2θ = 0.01° step and a counting time per step of 5 s. Analysis and refinement of the X-ray patterns were performed using the TOPAS Bruker software by applying the Le Bail method [30] and a Thompson−Cox−Hastings function for peak profile description [31]. For both samples, only *Fm*-3*m* phases were used for the refinement of the MOX materials. The 2θ zero-point deviation was corrected in the refinement by keeping the lattice parameter of the gold reference as a fixed variable (*Fm*-3*m* space group, lattice parameter of 4.0786 Å). For various reasons that will be detailed later in this paper, the lattice parameters extracted from the study of MOx samples will be given with an accuracy of 0.001 Å. Such an uncertainty is much higher than the ultimate one that can be reached with this instrument for pure phases.

C. EPMA

Spatially-resolved elemental analysis was conducted using a CAMECA SX100 microprobe. The electron beam acceleration was set at 20 kV and the probe current between 50 and 100 nA. Measurements were performed with four wavelength dispersive spectrometers (WDS) at the U Mα, Pu Mβ, Am Mα (using PET or L-PET type analyzer crystals: $C_5H_{12}O_4$, 2d = 0.874 nm) and O Kα lines (using an L-PC1 type multilayer analyzer: W-Si, 2d = 6.1 nm).

Two kinds of elemental mappings were recorded, referred to as large and detailed mappings. Large mappings are 1024 × 1024 pixels collected with horizontal and vertical steps of 1 µm obtained by sample stage displacement, with a counting time of 20 ms.stp^{-1}. Detailed mappings were collected on 100 × 100 µm^2 zones, with horizontal and vertical steps of 0.2 µm (hence 500 × 500 pixels), obtained by beam displacement, with a counting time of 100 ms.stp^{-1}.

Quantitative measurements were also performed in both samples along horizontal profiles of 300 to 700 µm with a 1 µm step obtained by sample stage displacement. The counting time was 15 s on the peak maximum and 5s for background measurements both before and after each peak. Mass fractions were measured using the PAP correction method [32] implemented in the CAMECA Peaksight software. Calibrations were performed on a UO_2 pellet for U Mα and O Kα and on a PuO_2 pellet for Pu Mβ. The interference of U Mγ line on the Pu Mβ line was taken into account through calibration on the same UO_2 pellet. For Am, as no standards were available, the calibration was performed on a $(Pu,Am)O_2$ "hotspot" of a heterogeneous $(U,Pu,Am)O_2$ pellet whose Am/(Pu+Am) of 9.2 wt.% was determined based on its isotopic composition and age. The absence of uranium in the spot selected for calibration was checked before recording the Am Mα intensity.

Pseudo-quantification of the plutonium EPMA mappings was performed by comparing the distribution of intensity counts in the elemental mappings and that of plutonium mass fractions extracted from the quantitative profile measurements. Porosity were identified as spots with low intensity of both U and Pu. A false color scale was used for the pseudo-quantification.

ACCEPTED MANUSCRIPT
Journal of Applied Physics
AIP Publishing
This is the author's peer reviewed, accepted manuscript. However, the online version of record will be different from this version once it has been copyedited and typeset.
PLEASE CITE THIS ARTICLE AS DOI: 10.1063/5.0103348

D. Raman spectroscopy

Raman spectroscopy was performed using a Horiba Jobin-Yvon iHR320 Raman spectrometer coupled to an optical microscope developed by Optique Peter (Lyon, France). Spectra were systematically recorded using a 100× objective. All the measurements were conducted using a 532 nm wavelength laser, along with a 1200 groove/mm^{-1} grating. Such a configuration *a priori* ensured an accuracy on the frequencies determination much better than 1 cm^{-1}. Light from a neon lamp was injected in the path of the scattered light to get a permanent frequency calibration of the spectrometer. Spectra were recorded over the wavenumber range from 90 to 1950 cm^{-1}. The incident power at the sample was adjusted to a few mW/μm^2 to avoid overheating and/or modification of the sample upon laser illumination. In particular, no clear evolutions of the spectra were observed after several acquisitions were run on the same spot, or when the power density at the sample was decreased. The spectrometer was calibrated using a silicon standard whose Raman line frequency has been fixed at 520.5 cm^{-1}.

The polarization of the scattered light was not analyzed. It was just verified that the setup had no strong polarization dependence, analyzing the response of the silicon standard for various angles between the polarization of the incident beam and the crystal axis. For these different orientations, the response of the silicon standard always remained almost constant.

The Raman images were systematically constructed with a measurement step of 2 µm, close to the actual spatial resolution of the method. For each acquisition point, the autofocus system of the instrument was used. The size of the examined areas (70 x 70 µm) was chosen to get, as far as possible, representative maps for each sample. Typical acquisition times of individual spectra were in the 30 to 100 s range, to get an "acceptable" signal to noise (S/N) ratio for each measurement point. This acquisition time had to be increased accordingly for the aged sample. Minimal spectra preprocessing was preferred because it may introduce some artifacts. Nevertheless, the light environment of the microscope was such that it was necessary to subtract its contribution in all the individual spectra. We verified that this subtraction did not add additional uncertainty to the measurements, in particular for the frequencies extracted from the individual spectra.

Afterwards, specific areas were identified in the images, and a few spectra were collected using much longer acquisition times, 300 s or more, to ensure to capture all the details of the spectra.

Data processing (reconstruction of images from the information present in all spectra, histograms, line fitting, acquisition of average spectra in some regions of the specimen) was achieved in part using the factory-supplied HORIBA Labspec 6 software. In particular, data averaging in specific regions (*i.e.* the constitutive agglomerates of the material) allowed significantly improving the S/N ratio of the spectra.

The same protocol was used to analyze the spectra of the aged and annealed samples, in particular for the determination of the frequencies. First, the integral intensity of the signal in

ACCEPTED MANUSCRIPT
Journal of Applied Physics
AIP Publishing
This is the author's peer reviewed, accepted manuscript. However, the online version of record will be different from this version once it has been copyedited and typeset.
PLEASE CITE THIS ARTICLE AS DOI: 10.1063/5.0103348

a selected spectral range were graphically computed for each sample. This is a very fast on-screen method, which allows an immediate examination of the results. Line intensity ratios were in part obtained in such a way. From one sample to another, the selected spectral ranges were strictly the same, which allowed the direct comparison of the corresponding images. Then, line fitting was also used to extract spectral features. This allowed, among other things, a better determination of the different intensity ratios. In such a case, all the individual spectra were first truncated in different regions of interest. Then, a linear background was subtracted. The signals were subsequently fitted with mixed functions (Gaussian + Lorentzian) of same frequencies and widths. Line fitting with such a function does not really make physical sense, but again, it allows to extract comparable quantities from one sample to another.

In general, the intensity of the signals used to reconstruct the images was relatively low. As a result, a first data survey has shown that the accuracy on the frequency determinations could not be better than about ± 0.3 cm^{-1}. This uncertainty is a parameter to take into account insofar small line shifts are to be evidenced in the following.

3. RESULTS

A. EPMA

EPMA was used to determine the distributions of U and Pu elements. On each metallographic cut, one region (1024 × 1024 pixels, ~ 1 mm^2) was randomly selected. An example of a pseudo-quantified Pu mapping is given in Fig. 1.a. It concerns the annealed sample. The full image is given, as well as a close-up that allows to determine the average sizes of the agglomerates, and to better distinguish the different phases. The trends obtained in terms of agglomerate sizes and Pu contents were similar for both the aged and annealed samples.

First, as expected, the method effectively enables the identification of the three so-called phases, *i.e.* the U- and Pu- rich agglomerates, as well as a region of intermediate composition, that is the coating phase. Basically, these phases are identified by the black, green and blue colors respectively in the EPMA image. The size of the U- and Pu-rich agglomerates is in the 10 - 30 µm range. From the image, the mean Pu content in each of the phases could be quantified. The analysis shows that Pu is mainly distributed between the Pu-rich agglomerates and the coating phase in which UO_2 and PuO_2 form a continuous solid solution. The average Pu/(U+Pu) content in the Pu-rich clusters is close to 30 wt%. However, the distribution of Pu is not completely homogeneous, including regions with lower contents, as well as small Pu-rich clusters indicated by the arrows in the image. The Pu content in the coating phase is uneven, mainly in the 5-20 wt% range. The Pu content in the U-rich agglomerates is rather close to the detection threshold of the method, about 1 wt%. Nevertheless, quantitative line scans (not shown here) show that this low Pu content is not constant within the U-rich agglomerates. More precisely, the Pu content is very low, below the detection threshold at the center of the bigger U-rich agglomerates, while it is rather observed in the 0-4 wt% range close to the edges of the agglomerates. Again, this is due to interdiffusion during sintering between the U-rich agglomerates and the PuO_2 contained in the coating phase.

ACCEPTED MANUSCRIPT
Journal of Applied Physics
AIP Publishing
This is the author's peer reviewed, accepted manuscript. However, the online version of record will be different from this version once it has been copyedited and typeset.
PLEASE CITE THIS ARTICLE AS DOI: 10.1063/5.0103348

Pu content histograms gave another description of the distribution of this element in the sample, see Fig. 1b. The histograms were constructed from the 1024 x 1024 pixels EPMA image. Three different regions may be distinguished in the histograms, centered at about 1, 9 and 29 wt%. These histograms confirm that the Pu distribution is rather heterogeneous. One can see in particular that the U-rich agglomerates have only a low average Pu content. The width of this first distribution suggests again that the Pu content is not constant in these agglomerates. A similar conclusion is reached for Pu-rich agglomerates. Finally, the comparison of the Pu content histograms of both aged and annealed samples confirms that the thermal treatment used for the defect healing did not significantly modify the Pu spatial distribution, see Fig. 1b.

EPMA provides a clear understanding of the microstructure of MOX fuels at the micron scale. From this point, it seems clear that the Raman data (images) are to be analyzed in a rather statistical way.

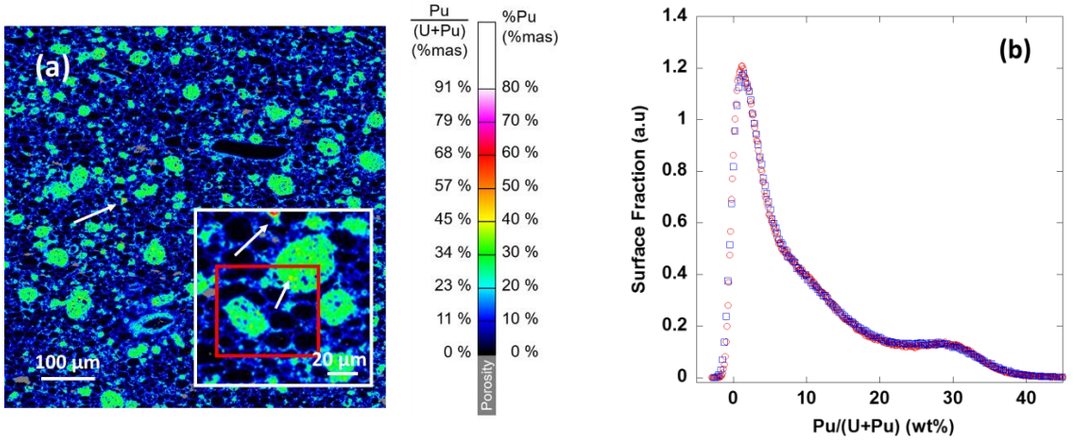

Figure 1: *(a) EPMA pseudo-quantified Pu large mapping in the annealed MOx MIMAS specimen. The white square is a detailed mapping of a particular region of the sample. The red square highlights a region in which the Raman analyses were conducted. Small clusters with very high Pu contents are indicated by the arrows. (b) Pu content histograms extracted from the Pu distribution image. Blue and red open circles correspond to the aged and annealed samples, respectively.*

B. XRD

XRD patterns of both specimens are given in Fig. 2. For comparison purposes, a characteristic diffraction pattern of $UO_{2.0}$ is also given. Here, the lattice parameter of $UO_{2.0}$ has been determined to 5.4708 Å, in close agreement with all previous works[33]. Analyses of XRD patterns show that both samples are only composed of *Fm*-3*m* fcc structure. As expected from the EPMA analysis, the diffraction line maxima of the annealed specimen are close to those observed for $UO_{2.0}$. Nevertheless, on the first reading, these diffraction patterns are to be adjusted by at least two different sets of lines, which can be seen more in detail in the inset of Fig. 2, see in particular the asymmetric broadening of the (111) reflection towards the high 2θ angles. This asymmetry obviously reflects the presence of the Pu-rich phases in the

ACCEPTED MANUSCRIPT
Journal of Applied Physics
AIP Publishing
This is the author's peer reviewed, accepted manuscript. However, the online version of record will be different from this version once it has been copyedited and typeset.
PLEASE CITE THIS ARTICLE AS DOI: 10.1063/5.0103348

specimens. Here, the two $k_{\alpha 1}$ and $k_{\alpha 2}$ reflections of Cu are clearly resolved. The lattice swelling upon self-irradiation is evidenced in the inset of Fig. 2 as a shift of the (111) reflection as a whole towards the lower 2θ angles. Another interesting point evidenced from Fig. 2 is the small effect of self-irradiation on the line widths. From the inset in Fig. 2, it is seen that the line width of the (111) reflection is quite similar for both aged and annealed samples. Considering the heterogeneous Pu content distribution evidenced by EPMA, and the resulting heterogeneous distribution in lattice parameters, the line width observed for both samples is rather small, notably when compared to that of the UO_2 reference sample. This means that micro-strains, in other words a distribution of local lattice parameters, remain rather low on average. Considering the context of this paper (only two samples were analyzed), we have not gone further in this analysis in terms of micro-strains.

To describe the diffraction patterns more in detail, several fluorite-type phases with close but different lattice parameters are to be used for the refinement. The use of only two phases proved to be insufficient to correctly model the experimental data, with a residue systematically indicating the presence of at least one other phase, whereas adding a fourth phase did not improve the fit. Three phases were further used for the refinements, assuming that the three different lattice parameters of the parent fluorite structure correspond to three different "mean" Pu contents. We are aware that this way of proceeding is a crude approximation insofar as the distribution of the lattice parameters is expected to be more or less continuous in view of the EPMA histograms. For this reason, we only give the different lattice parameters with an accuracy of 0.001 Å. This accuracy roughly corresponds to an uncertainty of about a few 10^{-4} on the average macroscopic strain, or of about 1 at% in terms of Pu content, assuming a simple Vegard's law, see Eq.3 below. This accuracy is therefore adequate to analyze the main effects of self-irradiation on the three different phases. It clearly allows revealing the main trends, in particular the average swelling of the 3 different phases, the main information required here. The refined lattice parameters of the aged and annealed samples are given in Table 3, along with the strain values induced by lattice swelling upon self-irradiation.

Table 3 *Mean lattice parameters extracted from the refinement of the XRD patterns. The Pu/(U+Pu) content was computed for the annealed sample lattice parameters using Eq. 3. The expected $\Delta a/a$ (%) were computed using Eq. 2 and the Pu content computed for the annealed sample.*

	U-rich agglomerates (Å)	Coating phase (Å)	Pu-rich agglomerates (Å)
Annealed	5.470(1)	5.466(3)	5.454(3)
Aged	5.482(1)	5.477(3)	5.473(3)
Pu/(U+Pu) (at%)	≈ 0	5.4	22
EPMA (wt%) Mean values	1 %	9 %	29 %

ACCEPTED MANUSCRIPT
Journal of Applied Physics
AIP Publishing
This is the author's peer reviewed, accepted manuscript. However, the online version of record will be different from this version once it has been copyedited and typeset.
PLEASE CITE THIS ARTICLE AS DOI: 10.1063/5.0103348

Δa/a (%)	0.22	0.20	0.34
Computed Δa/a (%)	0.12	0.29	0.29

Several information can be extracted from Table 3.

First, the lattice parameters of the annealed sample can be translated in terms of Pu content, according to the relation derived by Duriez et al. [5], which was further validated in the 0 < Pu < 0.46 range by Vauchy et al. [34]:

$$a = 5.470 - 0.074\,y + 0.32x \qquad (3)$$

where a (Å) is the lattice parameter, y the Pu/(U+Pu) molar fraction and x the difference to the perfect oxygen stoichiometry in $U_{1-y}Pu_yO_{2-x}$.

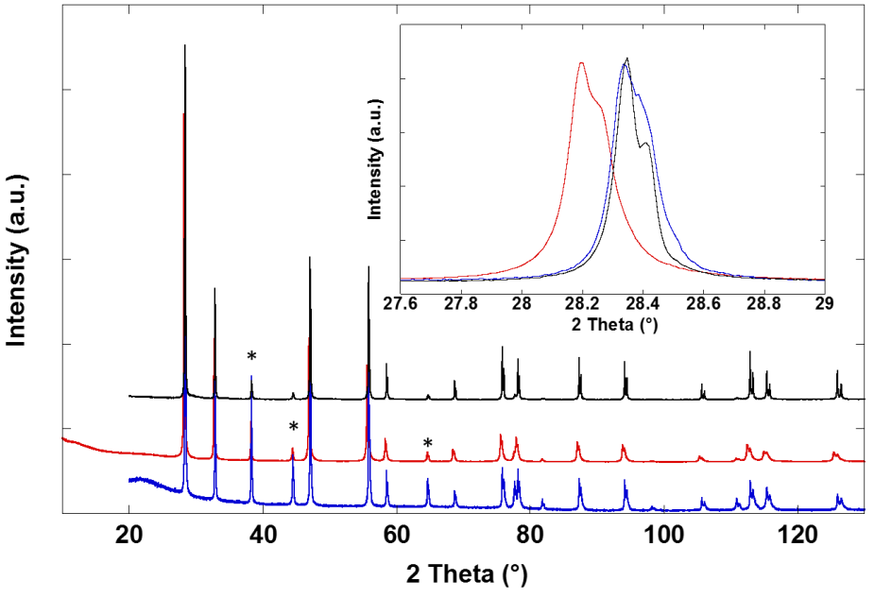

Figure 2 *XRD diffraction patterns of the aged (red line), annealed (blue line) and $UO_{2.0}$ (black line) specimens. The inset is a close-up on the (111) reflection. The asterisks indicate some of the reflections of the Au standard used for 2ϑ calibration purposes.*

Assuming oxygen stoichiometry throughout this work, the "mean" Pu content of the three phases, U-rich agglomerates, coating phase and Pu-rich agglomerates thus estimated using a Vegard's law between $UO_{2.00}$ (a ≈ 5.470 Å) and $PuO_{2.00}$ (a ≈ 5.396 Å) were found to be close to 0, 5.4 and 22. at%, respectively. One can see that the agreement with the mean values extracted from the EPMA histograms and given in Table 3 is quite satisfactory despite the approximations used and the large number of parameters left free during the fitting process. As a first approximation, these three lattice parameters can be considered as representative of the three phases.

ACCEPTED MANUSCRIPT
Journal of Applied Physics
AIP Publishing
This is the author's peer reviewed, accepted manuscript. However, the online version of record will be different from this version once it has been copyedited and typeset.
PLEASE CITE THIS ARTICLE AS DOI: 10.1063/5.0103348

The second information is the self-irradiation-induced swelling of the mean lattice parameter of the three phases. Whatever the phase, the amount of swelling falls in the 0.2 - 0.3% range, as expected from the literature. The last information is the swelling of the U-rich agglomerates. This means that these agglomerates capture the α radiation emitted by the other two phases. This is not surprising since the mean free path of α particles is about 10 µm in these materials.

C. Raman spectroscopy

The Raman spectrum of $(U_{1-y}Pu_y)O_{2.00}$ is known to exhibit a "one mode" behavior, *i.e*. it continuously evolves between that of UO_2 and that of PuO_2 [26,35]. This is not unexpected because of the small mass difference between U and Pu. An example of Raman spectrum (annealed sample, U-rich agglomerate) is given in Figure 3. It perfectly corresponds to the one collected on a $UO_{2.00}$ single crystal (see the blue line in the Fig. 3) using the same excitation at 532 nm, and more generally to those available in the literature, see Refs.[36,37]. Nevertheless, it is more complex than what is foreseen by group theory considerations insofar only one triply degenerated mode of T_{2g} symmetry is expected.

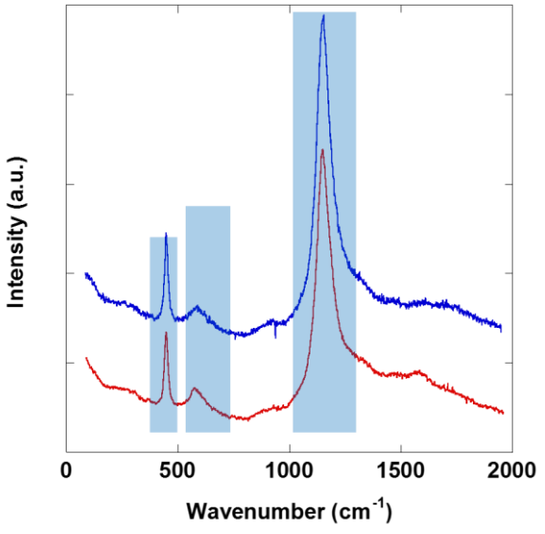

Figure 3 *Red line: example of Raman spectrum recorded within a U-rich agglomerate of the annealed sample. Blue line: characteristic Raman spectrum of stoichiometric $UO_{2.0}$, recorded using similar acquisition conditions on a single crystal. The frequency intervals highlighted in blue indicate the different regions of interest.*

The small difference in signal between the two spectra, in particular a weak maximum around 1600 cm^{-1} for the U-rich agglomerate is due to some residual carbon pollution[38], which comes from the metallization process, (the deposition of a few nanometer thickness layer of amorphous carbon at the sample surface) which is mandatory for the EPMA analysis of the samples.

ACCEPTED MANUSCRIPT
Journal of Applied Physics
AIP Publishing
This is the author's peer reviewed, accepted manuscript. However, the online version of record will be different from this version once it has been copyedited and typeset.
PLEASE CITE THIS ARTICLE AS DOI: 10.1063/5.0103348

From Figure 3, and up to 1200 cm^{-1}, five different bands and/or shoulders may be observed at about 445, 535, 576, 630, and 1150 cm^{-1}. We will not discuss the other signals (weak maxima at about 250, 900 and 1300 cm^{-1}) that most probably correspond to second-or higher-order scattering. More, their intensity is too weak to be used for the construction of the Raman images.

The first band is the Raman-allowed first-order mode with T_{2g} symmetry, observed at about 445 cm^{-1} for the U-rich agglomerates. In the absence of macro- or micro-strains, its frequency is related to the local Pu content (and O/(U+Pu) ratio, still assumed constant and equal to 2.00). It is known that the evolution of the frequency of this mode as a function of the Pu content can be described by a quadratic correlation, see Refs.[26,35,39]. Recently, Medyk et al. proposed the following empirical equation linking Pu/(U+Pu+Am) (y_t) content and T_{2g} (ω) position for O/M ratio equal to 2.00 [26]:

$$\omega = -1.221256 \times 10^{-3} \times {y_t}^2 + 0.452 \times y_t + 445.0 \qquad (4)$$

This quadratic correlation was derived for samples whose Am contents were in the 0.5 – 1.5 at% range, close to the values effectively found for the samples considered in this study, i.e. ≈ 1.9 at% in the Pu-rich agglomerates. Due to this very low content, the Am impact on the T_{2g} mode frequency can be safely ignored here, it can be considered that Eq. 4 refers to an Am-free material [40].

In the absence of strong micro- or macro-strains, is seen that the uncertainty on the determination of the Pu content is low, close to ± 1 at% considering the uncertainty discussed in the experimental part (± 0.3 cm^{-1}), *i.e.* an order of magnitude similar to that of EPMA or even XRD measurements. It is worth noting that this uncertainty would be lower in the case of analyzing a large number of data, as this is the case for the analysis of Raman images. Nevertheless, as it will be discussed later on, this is not the main cause of uncertainty here.

The hardening of the T_{2g} mode simply translates the decrease in the lattice parameter with the increase of the Pu content in the solid solution. In addition to the effects of structural disorder or even finite size effects, the width of this mode seems also slightly sensitive to the Pu content [26,35]. Both frequency and width images will be given, while the intensity of the T_{2g} mode, which does not bring here clear information on the orientation of the different grains as the polarization of the scattered light is not analyzed, will be mostly used for normalization purposes.

The prominent line at about 1150 cm^{-1} is known to be a specific second-order feature. Because this line is the second of a series of 6 lines peaking at about 575, 1150, 1725, 2312, 2910, and 3470 cm^{-1} [36], it is thus the first overtone of the 575 cm^{-1} line. This last frequency corresponds perfectly to the expected Raman-forbidden, IR-allowed LO line, see for example the computed dispersion curve available in Refs. [41–43]. Consequently, this line will be labelled 2LO, its corresponding first-order line 1LO. In what follows, the intensity of the 2LO mode will be normalized to the intensity of the T_{2g} mode, which is acceptable according to low polarization

ACCEPTED MANUSCRIPT
Journal of Applied Physics
AIP Publishing
This is the author's peer reviewed, accepted manuscript. However, the online version of record will be different from this version once it has been copyedited and typeset.
PLEASE CITE THIS ARTICLE AS DOI: 10.1063/5.0103348

dependence of the spectrometer used in this work. This intensity ratio will be referred as $2LO/T_{2g}$.

The last characteristic feature is a broad line centered at about the frequency of the 1LO mode (575 cm^{-1}), along with two more or less observable shoulders at 535 and 630 cm^{-1}. These lines are sometimes referred as a whole as the U* line, or as the triplet defect band (U^1, U^2 and U^3 respectively). The origin of these two shoulders on both sides of the 1LO mode, sometimes clearly seen as individual lines, is still being debated [21–26,35–37,39,44–48], while the observation of the Raman-forbidden 1LO mode is usually explained by the introduction of structural defects that lead to the loss of the inversion center of the fluorite lattice. This point will be discussed later in this paper. Again, in what follows, the intensity of the U* line (roughly the integrated intensity in the 500 – 750 cm^{-1} range) will be normalized to the intensity of the T_{2g} mode, and will be referred as a whole as U^*/T_{2g}.

Thus, four different Raman images can be used to track the self-irradiation effects. The annealed sample is analyzed first, see Fig. 4. As mentioned in the experimental part, the size of the images (70 x 70 µm) and the point spacing (2 µm) were chosen to analyze an area including agglomerates of the U-rich and Pu-rich phases, as well as zones that can be associated with the coating phase (as an example, see the EPMA image, Fig. 1.a), while looking for a compromise between acquisition time and signal quality. Again, the annealed sample is first assumed "defect-free" and "strain-free", still for simplicity and comparison purposes. One can note that this is a rather crude approximation as local micro-strains are unavoidable for this type of ceramics especially close to the grain boundaries[21]. Moreover, any deviation from the perfect oxygen stoichiometry may further complicate the analysis.

One can observe from Fig. 4 that three of the Raman images allow to immediately identify the different phases: the T_{2g} mode frequency, here directly translated in terms of Pu content, *i.e.* Pu/(U+Pu), the line width of the T_{2g} line and the $2LO/T_{2g}$ intensity ratio maps respectively. Accepting these simplifying assumptions, one can see that Pu/(U+Pu) concentrations are low, or even close to zero for the U-rich agglomerates and about 30% for the Pu-rich agglomerates. In the last case, small clusters with higher concentrations are also evidenced. On the other hand, one can see that the Pu content is not completely homogeneous in the different agglomerates. Furthermore, as expected from mass disorder considerations, the width of the T_{2g} mode is sensitive to the Pu content, even if the T_{2g} mode width image does not exhibit a very strong contrast. Quite surprisingly, the U^*/T_{2g} intensity ratio tends to highlight the coating phase.

ACCEPTED MANUSCRIPT
Journal of Applied Physics
AIP Publishing
This is the author's peer reviewed, accepted manuscript. However, the online version of record will be different from this version once it has been copyedited and typeset.
PLEASE CITE THIS ARTICLE AS DOI: 10.1063/5.0103348

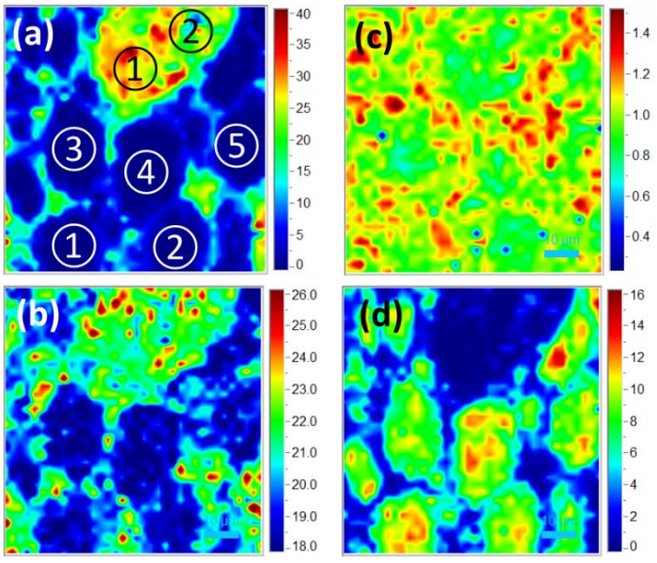

***Figure 4**: Images constructed from the Raman mapping of the annealed sample. The size of the images is 70 x 70 µm^2. (a): frequency of the T_{2g} mode, translated in terms of Pu/(U+Pu) content (at%). (b): line width of the T_{2g} mode (cm^{-1}). (c): U*/T_{2g} intensity ratio. (d): 2LO/T_{2g} intensity ratio. The white and black circles in Fig. 4.a indicate the agglomerates or regions for which spectra were averaged.*

A Pu content histogram has been obtained from the corresponding Raman image, that can be compared to the one obtained from the EPMA analysis, see Fig. 5. One can see that the agreement between the two data sets is basically satisfactory: the shape of the EPMA histogram is rather well reproduced. Hence, the quite small Raman image dimensions compared to EPMA are sufficient to observe the main characteristics of the sample microstructure.

Both methods give an average Pu/U+Pu content in the overall sample of ≈ 10%, which was the target Pu content during the synthesis process of this MIMAS-type sample. The small differences between the two histograms are not completely surprising considering the scale of the cationic heterogeneities in the sample and the comparatively small size of the Raman mapping. Other reasons, most probably of more fundamental origins, can also be evoked to understand the slight differences between the two methods. We will come back to this point afterwards.

ACCEPTED MANUSCRIPT
Journal of Applied Physics
AIP Publishing
This is the author's peer reviewed, accepted manuscript. However, the online version of record will be different from this version once it has been copyedited and typeset.
PLEASE CITE THIS ARTICLE AS DOI: 10.1063/5.0103348

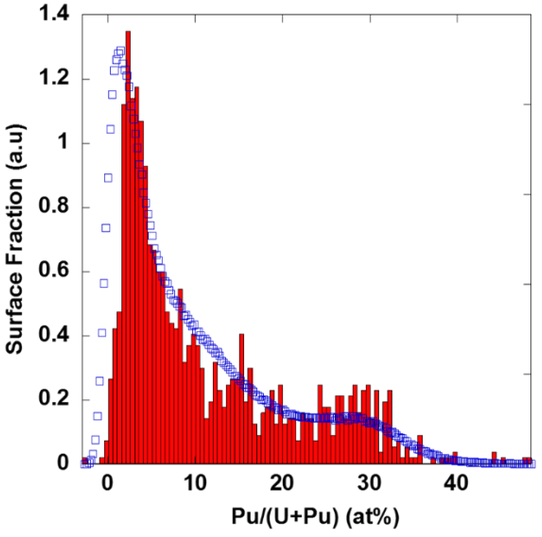

Figure 5: *Pu content histograms extracted from the EPMA (blue circles) and Raman (red bar graph) images.*

The corresponding images for the aged sample are given in Fig. 6. Here, the T_{2g} mode frequency cannot be translated in terms of Pu concentration as the frequency of this mode is sensitive to slight variations in the lattice parameter as shown in L. Medyk at al.[26] . Because of the cell parameter increase induced by self-irradiation, a downshift of this mode is indeed expected, this was one of the information sought.

On a first reading, the same microstructural trends are obtained. The four images still highlight the agglomerates even if the contrast of the images seems to be less pronounced. This phenomenon is perhaps a consequence of the lower S/N of the measurements. Two of the four images still allow to identify the different phases without too much ambiguity. More in details, the comparison of the T_{2g} width images (Figures 4b and 6b) suggests that self-irradiation induces a rather strong broadening of the band (on average 5 and 8 cm^{-1} respectively for the U- Pu- rich agglomerates). This broadening is observed for all three phases of the material. In addition, there is also a strong evolution of the U^*/T_{2g} intensity ratio, at least by about a factor 2, on average (Figures 4c and 6c). The strongest intensity ratios are now rather observed for the UO_2 clusters. Finally, it is seen from the figures that the $2LO/T_{2g}$ ratio is lower for the aged sample than for the annealed one, by about a factor of about 2 for the U-rich agglomerates (Figures 4d and 6d).

ACCEPTED MANUSCRIPT
Journal of Applied Physics
AIP Publishing
This is the author's peer reviewed, accepted manuscript. However, the online version of record will be different from this version once it has been copyedited and typeset.
PLEASE CITE THIS ARTICLE AS DOI: 10.1063/5.0103348

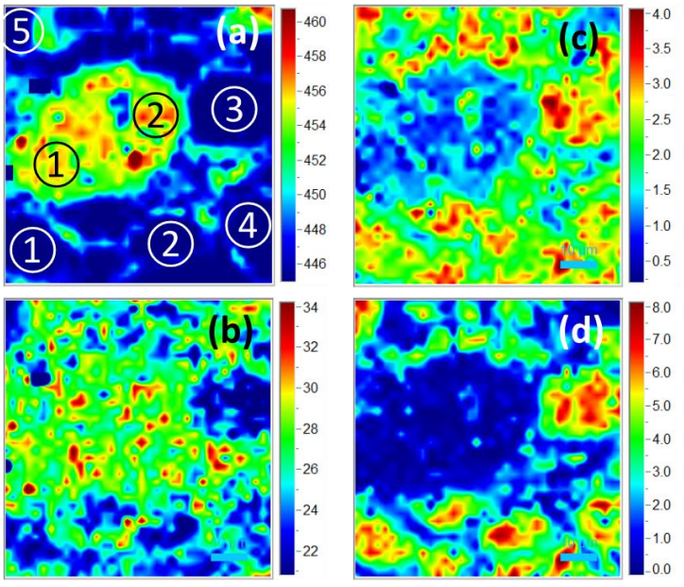

***Figure 6**: Images constructed from the Raman mapping of the aged sample. The size of the images is 70 x 70 µm². (a): frequency of the T_{2g} mode (cm^{-1}). (b): line width of the T_{2g} mode (cm^{-1}). (c): U^*/T_{2g} intensity ratio. (d): $2LO/T_{2g}$ intensity ratio. The circles in Fig. 6.a indicate the agglomerates or regions for which spectra were averaged.*

Therefore, these Raman images give the first trends. However, both U^*/T_{2g} and $2LO/T_{2g}$ maps seem to carry slightly different information.

Another way to analyze these images is to plot the width, U^*/T_{2g} and $2LO/T_{2g}$ parameters as determined for each pixel of the images as a function of the Pu content (annealed sample) and/or the T_{2g} mode frequency (aged sample). In fig. 7, one can examine the evolution, at least the mean trends of the U^*/T_{2g} and $2LO/T_{2g}$ evolution as a function of the Pu content. In other words, the evolution of these quantities can be examined in the 0 – 40 at% Pu concentration range using a single sample to analyze the Pu doping effect. Then, the effects of self-irradiation damage can be extracted in a more quantitative way by comparing aged and annealed samples.

First the evolutions of the $2LO/T_{2g}$ and U^*/T_{2g} intensity ratios are given in Fig. 7.a and 7.b respectively, as a function of the Pu content (annealed sample) or the T_{2g} mode frequency (annealed and aged sample). For both data sets, some spread is observed, unavoidable here because of the heterogeneity of the materials, the assumptions used, and the short acquisition time of the individual spectra. Nevertheless, rather clear trends are observed. In particular, Fig. 7.a shows a strong variation in the intensity of the 2LO mode as a function of Pu content. The intensity of this mode seems to be the highest for the lowest Pu concentrations, and decreases gradually thereafter. Above about 15 at% Pu/(U+Pu), the 2LO mode intensity is quite low and its decrease tends to slow down, while above 30%, it is very close to 0, the 2LO band being almost not clearly distinguishable in the individual spectra anymore. The same observation prevails for the aged sample, with an even faster decrease

ACCEPTED MANUSCRIPT
Journal of Applied Physics
AIP Publishing
This is the author's peer reviewed, accepted manuscript. However, the online version of record will be different from this version once it has been copyedited and typeset.
PLEASE CITE THIS ARTICLE AS DOI: 10.1063/5.0103348

for the smaller wavenumbers. On the other hand, self-irradiation induces a strong loss of intensity of this mode for low Pu contents, of about a factor 2. The behavior of the U* mode seems to be different as it tends to remain almost constant as a function of the Pu content for the annealed sample. A similar finding was already obtained in Ref. [35]. The self-irradiation amplifies the intensity of this mode for the lowest Pu contents, of about a factor 3. These results are to be discussed in terms of defect injection and resonant scattering.

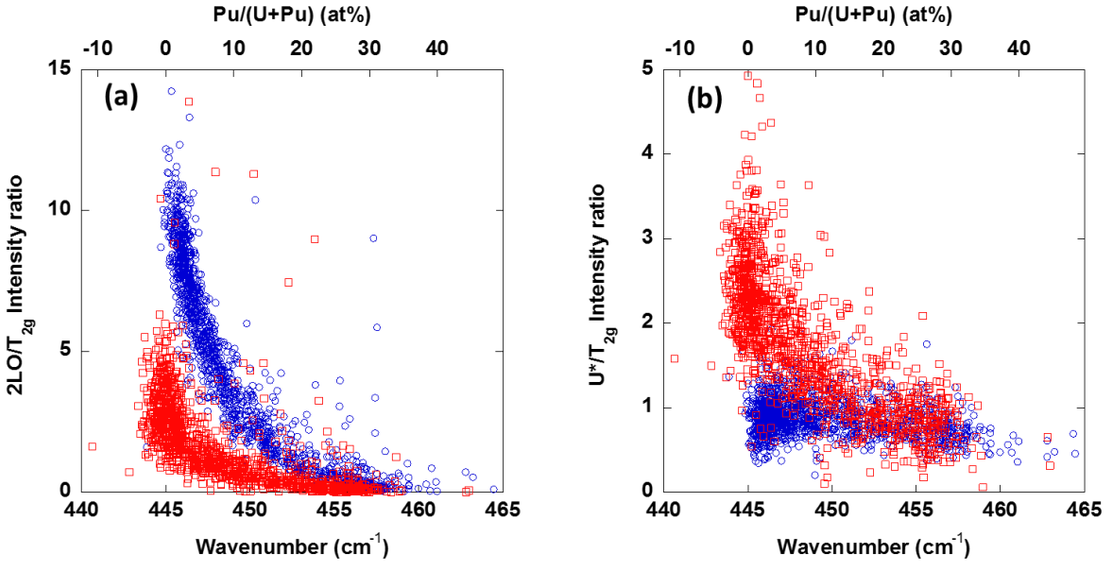

Figure 7*: (a): evolution of the 2LO/T_{2g} intensity ratio vs the Pu/(U+Pu) content (annealed sample, blue open circles) or the T_{2g} mode frequency (aged sample, red open circles). (b): evolution of the U*/T_{2g} intensity ratio vs the Pu/(U+Pu) content (annealed sample, blue open circles) or the T_{2g} mode frequency (aged sample, red open circles).*

In a similar way, one can finally focus on the evolution of two other variables, the T_{2g} mode width and the 2LO mode frequency, see Fig. 8. A small broadening of the T_{2g} mode is observed as a function of the Pu content, which probably reflects the mass disorder introduced by the Pu doping, see Fig. 8.a. Indeed, this line width was found to be close to 13 cm^{-1} for a freshly annealed $PuO_{2.0}$ sample on the same experimental setup. It should be noted here that only the trend is to be considered, the absolute values of the line widths depending on the spectrometer used and the measurement conditions. From Fig. 8.b, a small hardening of the 2LO mode, of about 3 cm^{-1} for a Pu content close to 30 at%, can be discussed. This hardening remains weak compared to that of the T_{2g} mode, close to 12 cm^{-1} for a similar Pu content. The 2LO mode is effectively peaking at about 1160 cm^{-1} for PuO_2. The main consequence of this low frequency variation is probably that it will be almost unobservable on the 1LO mode, which is generally observed.

ACCEPTED MANUSCRIPT
Journal of Applied Physics
AIP Publishing
This is the author's peer reviewed, accepted manuscript. However, the online version of record will be different from this version once it has been copyedited and typeset.
PLEASE CITE THIS ARTICLE AS DOI: 10.1063/5.0103348

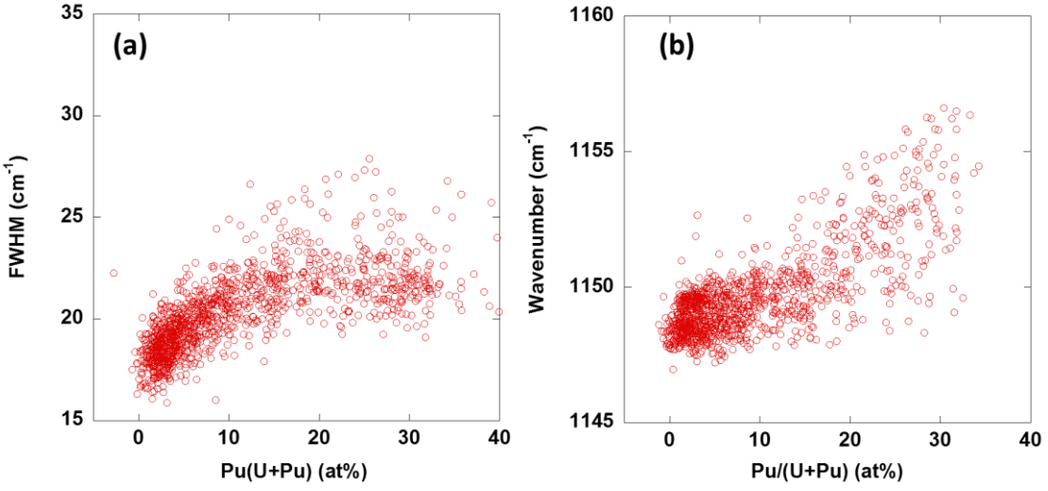

***Figure 8**: (a): evolution of the width of the T_{2g} mode in the annealed sample vs the Pu content. (b): evolution of the frequency of the 2LO mode in the annealed sample vs the Pu content*

To retrieve the last information, it is necessary to analyze the spectra in more detail. For such a purpose, it first seems convenient to use average spectra obtained on predefined areas, or particular agglomerates that were already evidenced and identified in the frequency images, at least to increase the S/N ratio of the signals. These agglomerates are highlighted in Fig. 4 and Fig. 6. Examples of such averaged spectra are given in Fig. 9.

Two and five spectra could be extracted for the Pu- and U-rich agglomerates, respectively. A first information is the strong signal loss for the self-irradiated sample. This signal loss is reflected by the low S/N ratio of the corresponding spectrum. In both cases, a strong broadening of the T_{2g} mode is evidenced upon self-irradiation. This strong broadening has already been suggested by several authors [22,48,49]. An asymmetry of this mode towards the low frequencies can also be discussed. A small, but detectable, downshift of the T_{2g} mode seems to be observed in a systematic way. We come back to point this below.

The evolution of the U* line as a whole is more dependent on the Pu content of the agglomerates. When normalized to the T_{2g} mode intensity, it only increases slightly for Pu-rich agglomerates, an information buried in the noise of the measurement if we consider all the individual spectra, see Fig. 7.b. On the contrary, a strong increase in intensity is observed for U-rich agglomerates, as already shown in Fig. 7.b. Finally, in both cases, a shoulder at a lower frequency from the forbidden 1LO mode (the U^1 line) clearly stands out from the U* signal, see the arrows in Figs. 9.b and Figs. 9.d.

ACCEPTED MANUSCRIPT
Journal of Applied Physics
AIP Publishing
This is the author's peer reviewed, accepted manuscript. However, the online version of record will be different from this version once it has been copyedited and typeset.
PLEASE CITE THIS ARTICLE AS DOI: 10.1063/5.0103348

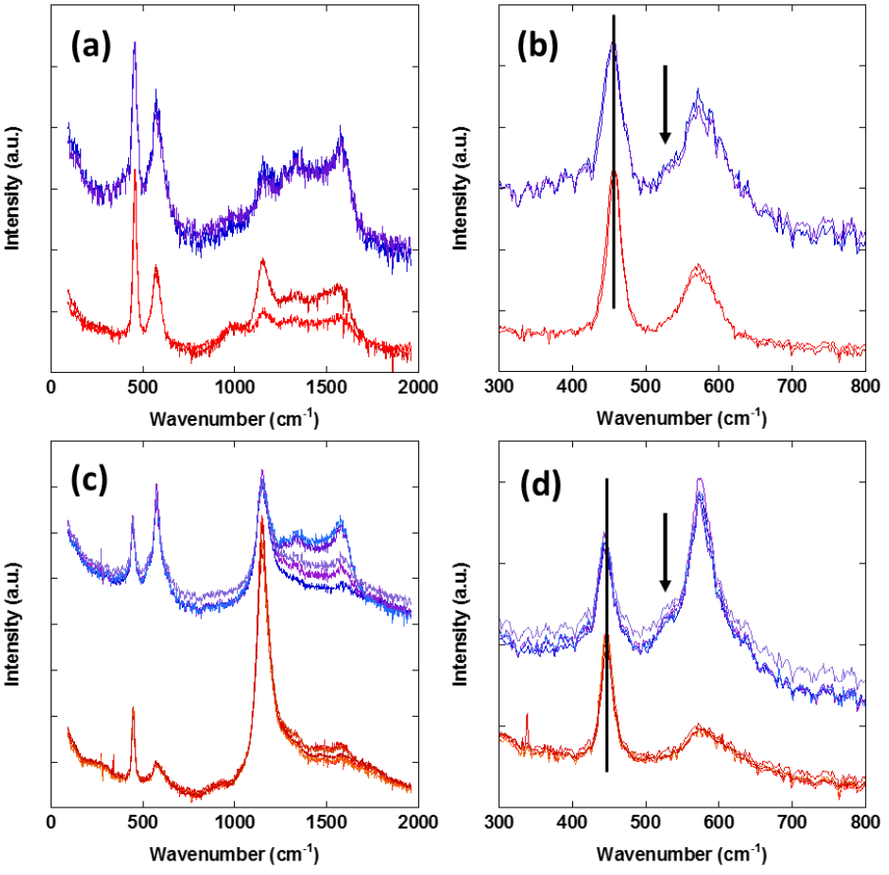

Figure 9*. Examples of averaged Raman spectra for Pu (a and b)- and U- rich (c and d) agglomerates. The zones from which these signals have been extracted are indicated in Fig. 4a and 6a, respectively. Reddish lines correspond to the annealed specimen; bluish lines correspond to the aged specimen. (a) and (c): complete spectra, between ≈ 100 and ≈ 2000 cm-1. (b) and (d): close-up of the first order region. The arrows highlight the U1 signal, clearly detected for the aged sample.*

Line fitting of the spectra, of the T_{2g} mode in particular, gives the last trends. The mode frequency and width is given in Fig. 10 for the two Pu rich- and the five U-rich agglomerates. The fitting process allows to quantify the visual examination of the spectra, see Fig. 9. One can see that the agglomerates are not all rigorously equivalent, perhaps a consequence of the choice of the areas from which the spectra have been averaged. However, on average, one observes downshifts of about 2.2 and 1.6 cm^{-1} for the Pu- and U-rich agglomerates, respectively, whereas broadenings of 11 and 8 cm^{-1} are observed for the same zones.

ACCEPTED MANUSCRIPT
Journal of Applied Physics
AIP Publishing
This is the author's peer reviewed, accepted manuscript. However, the online version of record will be different from this version once it has been copyedited and typeset.
PLEASE CITE THIS ARTICLE AS DOI: 10.1063/5.0103348

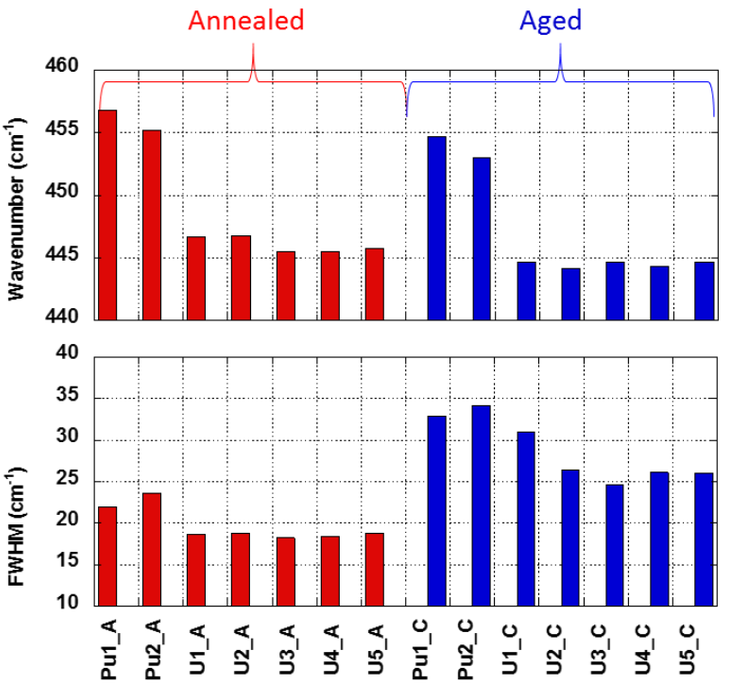

***Figure 10**. Frequency and width of the T_{2g} mode for U- and Pu- rich agglomerates. Corresponding spectra are plotted in Fig. 9.*

4. DISCUSSION

The mid-term rationale behind the present study is to track and analyze self-irradiation effects in a particular MOx fuel of the MIMAS type. In a first step, a combination of three techniques (EPMA, XRD and RS) was used to track these irradiation effects for two specific samples, for which it was first assumed that these effects were maximized or minimized.

One of the macroscopic effects of self-irradiation is the material(s) swelling. XRD confirmed this swelling for the three main phases of this particular fuel, close to 0.3% as suggested by all previous studies. It is therefore not necessary to comment further on this experimental evidence. We just point out that the kinetics of this swelling most probably depends on the phase concerned. Similarly, one can think that the irradiation effects are induced by both recoil nuclei and α particles in the Pu-rich areas, whereas in the U-rich agglomerates they are mainly induced by α particles from Pu present in the surrounding coating phase and or Pu-rich agglomerates. This explains the discrepancy between the very low Pu content (<0.5 wt.%) estimated from the lattice parameter of the U-rich phase of the annealed sample and the large swelling observed for this same phase in the aged sample (≈ 0.2%). For this phase, one might consider that a significant part of the cumulated α dose results from Pu present in the surrounding coating phase.

The present results also show that some of the self-irradiation effects in MIMAS-type fuels can be tracked through some modifications in the Raman spectra, what was less documented in

ACCEPTED MANUSCRIPT
Journal of Applied Physics
AIP Publishing
This is the author's peer reviewed, accepted manuscript. However, the online version of record will be different from this version once it has been copyedited and typeset.
PLEASE CITE THIS ARTICLE AS DOI: 10.1063/5.0103348

the literature. These changes were evidenced by comparing the U- and Pu-rich agglomerates before and after annealing of the material. This is what we will try to discuss more in detail in what follows.

A. The present approach: main limitations of the assumptions used

From a methodological point of view, imaging methods have been used. Data can therefore be analyzed more or less in a statistical way, which is a known advantage for the analysis of heterogeneous materials. The data may appear noisy at first sight, which is due to (i) the measurement environment, (ii) the need to analyze a representative area of the sample in a given time frame (Raman imaging is always a matter of compromises between acquisition time and signal quality), (iii) most importantly the compositional and the likely mechanical heterogeneity of the sample. The availability of a large amount of data allows the extraction of trends. Raman imaging was used for this purpose, even if the number of agglomerates of the different phases accessible to the measurement, about ten at most, remains relatively modest. We are aware that this may call into question some of the trends identified thanks to use of this technique. Nevertheless, only the U- and Pu-rich agglomerates have been analyzed in detail. For these agglomerates, the EPMA images tend to demonstrate that they have rather similar characteristics in terms of Pu content, see in particular the color encoding of the EPMA images. We therefore believe that the observed trends can be accepted, which confirms that this technique can be relevant for the study of actinide oxides, as already suggested by many works [21–25], taking into account the impact of the analysis wavelength, as we will see below.

RS is increasingly used to monitor self-irradiation damage over time. As more or less expected from the literature survey, self-irradiation leads to different modifications of the Raman spectra for the three constituent phases. Still from a methodological point of view, the first point to take into account is the wavelength at which the analyses were conducted: 532 nm. It is known that for such wavelength, UO_2 Raman signal is resonant, and that these conditions are expected to be lost above a Pu/(U+Pu) content of about 15 at%. We will come back to this point below. Therefore, all three phases are not probed in the same way. Indeed, in resonant conditions, the penetration depth is necessarily reduced. It is difficult to get a more precise idea of this penetration depth as the literature data show a large spread in the optical constants. According to published extinction coefficient values [50–54], it is most probably much lower than one µm, with enhanced consequences of any surface modification. Moreover, the penetration depth is probably not constant over the analyzed surface, being larger for the Pu-rich areas.

From the analysis of the Raman images, it appears that four different spectral features bring information, namely the T_{2g} mode frequency and width and perhaps its slight asymmetry, the 2LO intensity, and finally the U* intensity and its line shape, that are to be discussed in terms of strain, defect injection, and resonant scattering.

ACCEPTED MANUSCRIPT
Journal of Applied Physics
AIP Publishing
This is the author's peer reviewed, accepted manuscript. However, the online version of record will be different from this version once it has been copyedited and typeset.
PLEASE CITE THIS ARTICLE AS DOI: 10.1063/5.0103348

B. T_{2g} mode frequency and width

Focusing on the T_{2g} mode, the only Raman-allowed mode from the first-order selection rules, it can be seen that self-irradiation first induces a strong broadening of this mode, which was already documented for UO_2, PuO_2 as well as for $(U,Pu)O_2$ [22,48]. It also seems to induce a mode downshift, which has not been systematically reported. Finally, as already suggested [22,48], a small asymmetry of this mode towards the low frequencies seems to be detected. First, these characteristics may have experimental origins, overheating and/or hypo-stoichiometry [26] of the aged sample. In particular, self-irradiation is known to lead to some decrease of the thermal conductivity of the MOx material. Such a decrease in the thermal conductivity may affect the temperature reached by the sample under the focused laser beam. We are aware that both origins cannot be completely ruled out, even if, from an experimental point of view, many precautions have been taken, see the experimental part of the paper.

If these experimental origins are disregarded, the downshift of this mode can *a priori* be explained in two different ways. The first approach is to consider that the mode softening directly translates the lattice expansion or swelling, in other words the strain of the material induced by its self-irradiation. Different approaches can be used to relate strain to Raman shifts. Within the scope of this paper, the most intuitive one is most probably the use of the so-called Grüneisen parameter. In its microscopic formulation, the Grüneisen parameter γ is a measure of how a specific phonon frequency is altered under a small change in the geometry of the crystallographic unit cell. For isotropic materials, or materials with cubic lattice symmetry, the Grüneisen parameter is simply a scalar that refers to an isotropic change in the volume *V*, according to [55]:

$$\frac{\Delta\omega}{\omega_0} = -\gamma\frac{\Delta V}{V_0} \approx -3\gamma\frac{\Delta a}{a_0} \qquad (5)$$

where ω_0, V_0 and a_0 are the vibrational frequency, unit cell volume and lattice parameter under ambient pressure and temperature conditions, and $\Delta\omega$, ΔV and Δa are the corresponding changes with pressure and/or temperature. As a rule, the Grüneisen parameters are close to unity. When the so-called "anharmonic effects" are low, the dimensionless Grüneisen parameter should be similar for isothermal and isobaric lattice parameter changes, as it was observed for CeO_2 [56], another material crystallizing in the fluorite structure. There are only few data in the literature that give estimates of the Grüneisen parameter for UO_2 [22,36]. This parameter is usually obtained examining samples vs temperature or isostatic pressure. A first overview of the available data shows a strong scattering of these values, 1.28 or 2.2 according to Refs [22,36] respectively. The analysis of the few data available that give the T_{2g} mode frequency vs temperature, see Refs [57,58], leads to another, but much lower value, close to 0.5. In any case, only an order of magnitude is necessary here, since there is no reason why the elastic properties of virtually defect-free and irradiated materials should be strictly the same. Eq. 5 shows that this order of magnitude is close to a few cm^{-1} for a strain value of 0.3%. This order of magnitude effectively matches the observed T_{2g} mode downshift

ACCEPTED MANUSCRIPT
Journal of Applied Physics
AIP Publishing
This is the author's peer reviewed, accepted manuscript. However, the online version of record will be different from this version once it has been copyedited and typeset.
PLEASE CITE THIS ARTICLE AS DOI: 10.1063/5.0103348

values. Accepting this assumption, the frequency of the T_{2g} mode reflects the swelling of the material, while the T_{2g} mode width reflects defect injection.

The T_{2g} mode downshift might also be a direct consequence of the introduction of point or extended defects in the crystal lattice, that may induce a partial or a complete relaxation of the $k \approx 0$ selection rule. This is consistent with the fact that both molecular dynamic simulations ref.[18,19] and TEM observations ref.[3,13] show that point defects progressively arrange themselves into dislocations, creating nano-domains. When the amount of defects is quite large, inducing small characteristic lengths or mean coherent sizes below ≈ 15 nm, these effects are usually discussed according to the phenomenological phonon confinement model[59], also known as the spatial-correlation model. Depending on the dispersion of the optical branches in the Brillouin zone, a shift and asymmetrical broadening of the Raman-allowed line may be observed. The disorder transforms sharp Raman lines, resulting from wavevector (*k*) conservation in crystals, into phonon densities of states induced-features. The range of phonon wave vectors that contributes to the Raman line shape is determined by the mean crystallite size, or even the mean distance between defects, and is usually approximated by $\Delta k \approx 2\pi/l$, where *l* is a characteristic length. These confinement effects have been widely discussed for most semiconductor materials [60] and more interestingly here for CeO_2 [61]. In the latter case, it was clearly observed that the T_{2g} mode of the CeO_2 nanoparticles shifts progressively to lower energies while the line shape of this feature gets progressively broader and asymmetric on the low-energy side as the particle size gets smaller, below ca 15 nm. As the examination of the phonon dispersion curves [41–43] shows a strong bending of the LO1 branch towards the low frequencies, this hypothesis cannot be completely ruled out. The T_{2g} mode downshift observed here would show that the characteristic length (a mean distance between defects) is effectively lower than 15 nm, what is not known here, and even perhaps unlikely as the diffraction patterns do not show specific line broadening.

One note that both origins, strain and confinement, cannot be easily discriminated here.

The analysis of the swelling process supposes to know the local Pu content, and even the local stoichiometry. This is quite tricky here since the Pu content was found to be highly heterogeneous: not all µm spots have constant and same rigorously exact concentrations. This is why, in our opinion, a statistical analysis was necessary, at least on the basis of the analysis of a few areas as in the present study. The frequency of the T_{2g} mode was also used to track the local Pu content in the annealed material, using two strong assumptions: absence of micro-strain and exact stoichiometry. The comparison of the Raman and EPMA data was quite satisfactory, as shown by the comparison of both Pu content histograms. It could be even better by simply slightly adjusting the parameters of eq. 4, *i.e.* the initial mode frequency and the equation that describes the variation of the mode frequency with the Pu content. Nevertheless, taking into account the uncertainty on the determination of the frequencies (± 0.3 cm^{-1}) and the rather limited set of experimental data available to establish Eq. 4, this relation is probably a first acceptable approximation. The effect of the oxygen hypo-stoichiometry x on the T_{2g} mode frequency can be readily assessed. It is similar to that of a

ACCEPTED MANUSCRIPT
Journal of Applied Physics
AIP Publishing
This is the author's peer reviewed, accepted manuscript. However, the online version of record will be different from this version once it has been copyedited and typeset.
PLEASE CITE THIS ARTICLE AS DOI: 10.1063/5.0103348

decrease in Pu content, along with a downshift of the T_{2g} mode of about 2 cm^{-1} for a hypo-stoichiometry close to 0.01 [26]. Nevertheless, irrespective of the consequences of deviations from exact stoichiometry, strain effects are also to be discussed. It seems obvious that two types of strains are to be taken into account here: micro-strains, always present in this type of ceramics, for example along grain boundaries, as well as more "macroscopic" strains, for example induced by differential grain volume variations during the sintering process or even during the material swelling (in other words, it was assumed that the swelling was homogeneous in the material). Both origins cannot be completely excluded here. An order of magnitude of the micro-strain effects can be obtained by Raman imaging a representative area of a stoichiometric UO_2 pellet, which was done in Ref. [21]. The contrast of the frequency images was found to be close to 3 cm^{-1}. Translated in terms of Pu concentration according to Eq. 4, one can immediately see that locally, the uncertainty on the local Pu content can be as large as 4%. The consequences of the synthesis process cannot be simply evaluated and discussed here, but one can anticipate similar consequences in terms of uncertainty on the Pu content. Neglecting strain effects is therefore a rather strong assumption.

C. The 2LO mode intensity

The analysis of the other characteristic signals of the individual spectra also gave some information. The intensity of the 2LO mode could be used to localize U-rich agglomerates, and discriminate them from Pu-rich agglomerates. As such, this information is not completely new, see for example Refs. [13,22,26]. This mode is a second-order, overtone mode, therefore *a priori* Raman-allowed, without disorder consideration. For pure UO_2, the Raman excitation profile of this mode has been published very recently [37]. It is centered on 2.3 eV approximately, that is very close to the energy of the excitation used in the present investigation (2.33 eV). The Raman excitation profile was observed to be quite narrow, 400 meV at most. More, this mode is known to be polarized, being mostly observed for parallel polarizations of the incident and scattered beams. This can be rather important from an experimental point of view: not all spectrometers have the same response to polarized light. Both the resonance enhancement and the polarization dependence of the LO line series are in agreement with a mechanism based on the Fröhlich electron-phonon interaction, as observed and discussed previously for polar semiconductors such as CdS, ZnO, or GaN.[36,62,63]. The resonance conditions are intuitively expected to be related to the optical properties of the alloys, the position of the absorption edge in particular. The absorption edges of UO_2 and PuO_2 were determined, they were observed close to 2 and 2.6 eV respectively [54,64]. Due to the steepness of the resonance profile, these specific conditions are expected to be quickly lost while the solid solution is progressively enriched in Pu, beyond about ca 15 at% Pu/(U+Pu) if one accepts a linear evolution of the absorption edge with the composition, in a first crude approximation. This is more or less what the Raman images and Fig. 7.a have shown. Moreover, the examination of the spectra shows that the intensity of this mode strongly decreases with the injection of defects in the fluorite lattice and the resulting swelling of the lattice parameter. This fact has been extensively reported in previous studies [22,26,48,49,65]. It is known that the absorption edge

ACCEPTED MANUSCRIPT
Journal of Applied Physics
AIP Publishing
This is the author's peer reviewed, accepted manuscript. However, the online version of record will be different from this version once it has been copyedited and typeset.
PLEASE CITE THIS ARTICLE AS DOI: 10.1063/5.0103348

is strongly shifted with pressure, temperature and even hyper- or hypo-stoichiometry. First, one can first think that the absorption threshold is red-shifted with the increase of the lattice parameter, in a way similar to what has already been observed with temperature [35]. More, the introduction of structural defects most probably leads to a same finding, without formal proof however. Another consequence of the introduction of structural defects is most probably to blur or smooth out the resonance conditions. The loss of intensity of this mode thus effectively tracks any deviation from the perfect $UO_{2.0}$ fluorite structure, in an indirect way however, because these are the electronic properties that are predominantly probed here through the intensity of this mode.

D. The 1LO mode, the U^1 and U^3 signals.

The last characteristic feature of the $(U,Pu)O_2$ Raman spectrum is clearly the U* group of lines. This group of lines is clearly dominated by the "Raman-forbidden" 1LO mode. Most of the time, this group of lines is also referred as a "Raman defect-induced spectrum". Even if the 1LO mode implies a small amplitude movement of the cation, these lines fall if a frequency range for which vibrational modes are oxygen-dominated, see for example the O and U partial phonon density of states available in Refs. [42]. This characteristic signal is not a unique characteristic feature of actinide oxides, being observed in part for ceria [56,66]. The 1LO mode, as well as the U^1 and U^3 lines, is also resonance enhanced, again, a scenario to be attributed to the Fröhlich electron - phonon interaction. In most cases, using resonant excitation conditions in particular, the intensity of the 1LO mode seems to overwhelm that of U^1 and U^3 modes, preventing their clear observation. Nevertheless, it is not clear whether the U^1 and U^3 modes have a similar resonance profile to the 1LO and 2LO modes. It seems not, based on Ref [67]. A similar finding was clearly reported for PuO_2 [68].

It is generally accepted that the 1LO mode finds its origin in deviations from the perfect fluorite structure. It is in fact a proof of the breakdown of the inversion symmetry. Therefore, it is understandable that the presence of any structural defect, point as well as extended, is sufficient to activate this mode. More, in the case of a solid solution such as the one presently considered, it seems clear that all the Pu-O and U-O distances are not strictly equivalent, which was confirmed by EXAFS measurements [45]. One therefore intuitively expects an increase in the intensity of the 1LO mode enriching the solid solution in Pu, while, at the same time, the resonance conditions are progressively lost. This is probably the reason why the intensity of this mode seems to remain almost constant during the Pu enrichment of the solid solution, see for example [35]. This may also explain the differences observed in the $1LO/T_{2g}$ intensity ratio images for the annealed and aged samples, the maximum intensity of this ratio being rather observed in the coating phase in the first case, in the U-rich agglomerates in the second, due to defect injection and variations in resonant scattering conditions. One also sees that a similar reasoning allows to explain why this signal is also observed for slightly hyper stoichiometric UO_{2+x} [69], the lattice distortions arising from differences in the ionic radii between the different oxidation states of the U cations that allow charge balance (and thus differences in U^{4+}-O and U^{5+}-O distances) and the presence of O interstitials.

ACCEPTED MANUSCRIPT
Journal of Applied Physics
AIP Publishing
This is the author's peer reviewed, accepted manuscript. However, the online version of record will be different from this version once it has been copyedited and typeset.
PLEASE CITE THIS ARTICLE AS DOI: 10.1063/5.0103348

When using the 2LO and U* modes, the important finding is that not all areas are analyzed in a similar way, and that not all spectral characteristics carry the same information, depending on the Pu content. As a matter of fact, the intensity of the 2LO and U* modes does not allow to completely track the effects of self-irradiation beyond a Pu content of about 15 at%. Indeed, the spectra are seen to be rather similar in shape before and after self-irradiation, see Fig. 9. More, it is seen the intensity ratios are no longer completely discriminating, see Fig. 7. Only a small increase in the U^*/T_{2g} ratio seems to be observed, based on the analysis of two agglomerates. On the contrary, for the lowest Pu contents, the intensity of the 2LO and U* modes is clearly discriminating, and can be used to monitor self-irradiation effects with a high sensitivity, along with the width and most probably the frequency of the Raman allowed T_{2g} mode, even if the irradiation damage-induced variations are moderate. To probe all the agglomerates in a similar way, it therefore appears necessary to use an excitation well below the absorption threshold of UO_2, that is in the near infrared region, and to accept to completely lose the information carried by the 2LO and U* modes. Another way to proceed might be to use three different excitations, in order to probe resonantly the U- and Pu-rich agglomerates as well as the coating phase, using wavelengths in the blue and violet spectral range. Such excitations were not available for the present study.

The U^3 shoulder was always observed, or at least suggested by the adjustment of the U* signal into three resolved components, for all the spectra. On the other hand, the U^1 shoulder seems to be mostly observed after self-irradiation. According to Ref. [35], neither of the two peaks seem to shift with the excitation energy, as expected for a first-order mode. Literature shows that the relaxation of the $k \approx 0$ selection rule due to defects or finite crystallite size not only broadens the Raman allowed modes, but can also cause new modes to appear, which may correspond *to* $k \neq 0$ phonons. Here, a prototypical example is graphene [70]. Nevertheless, the frequencies of U^1 and U^3 modes do not clearly correspond to the maxima observed in the computed or measured density of state curves, see Ref. [39] . More, U^3 mode frequency seems to lie slightly above the cut-off frequency of the PDOS, whereas U^1 is rather observed in a forbidden frequency gap between the LO2 and TO2 branches. One can therefore assume that these two signals have different origins, and more importantly that they are not zone-edge modes of the perfect fluorite structure that are activated by some relaxation of the $k \approx 0$ selection rule. Nevertheless, it is known that point defects usually change the vibrational structure of a solid. Both U^1 and U^3 mode are therefore most probably induced by the presence of at least two specific structural defects, or at least two defects with different atomic environments around it. Most probably, they cannot be considered as "local" modes insofar as their frequencies rather overlap with the bulk phonon spectrum, and thus they are not strictly localized in space. Interestingly, similar signatures were reported for hypo-stoichiometric CeO_{2-x}. Bands in the 480−600 cm^{-1} region were observed and associated with the presence of oxygen vacancies accompanied by the formation of reduced Ce^{3+} sites. More in details, Density Functional Theory (DFT) computations revealed that that the coordination cube around $Ce^{4+/3+}$ ions in hypo-stoichiometric CeO_{2-x} strongly influences the spectral properties [66]. In particular, it was shown that in the Raman spectra of bulk CeO_{2-x}, a clear

ACCEPTED MANUSCRIPT
Journal of Applied Physics
AIP Publishing
This is the author's peer reviewed, accepted manuscript. However, the online version of record will be different from this version once it has been copyedited and typeset.
PLEASE CITE THIS ARTICLE AS DOI: 10.1063/5.0103348

distinction could be made between Raman bands arising from Ce^{3+} in direct proximity to the oxygen defect, characterized by a computed band at 500 cm^{-1}, and those originating from Ce^{3+} located in the second coordination sphere of the oxygen vacancy, giving rise to a band at 480 cm^{-1}. Since the crystal structures are similar, with more or less the same vibrational spectra, it is not unreasonable to look for a similar explanation for actinide oxides.

Finally, it should be noted that some works associate the U^3 line with the presence of U_4O_9 on the surface of the samples, translating a slight surface oxidation. Even if it cannot be totally rejected, it seems difficult to accept this hypothesis since the U^3 signal, or at least a signal with a similar frequency, is observed for PuO_2. Such a phase is unknown in the Pu-O binary diagram. More, this signal was found to be resonantly enhanced using an excitation at 785 nm [24]. This is most probably not the case here.

In any event, it seems completely unrealistic to assume that there are only two types of defect environments in such a self-irradiated ceramic material. The irradiation leads indeed to the creation of plenty of point and extended defects, with different environments. The U^1, U^2 and U^3 signals have been found for different situations: annealed, polished, irradiated material, grain boundaries in a ceramic. In all cases, the intensity of these signals depends on the excitation wavelength and on the thermal history of the material. It is therefore not unreasonable to assume that the Raman analysis probes only two specific defect environments, with their own specific electronic energy levels, that are tuned close to the excitation energy during Raman measurements. It remains to determine what are these defects environment. Clearly, DFT-based computations seem necessary propose some scenarios.

E. Am enrichment

Another effect of self-irradiation, not completely discussed so far, is the enrichment in Am. This enrichment, close to a factor of five, is reflected in both samples. As a matter of fact, the spatial distribution of Am in the sample has to follow that of Pu, which was recently verified using x-ray fluorescence mapping. It is thus expected that the main consequences of this Am enrichment are to be found in the Pu rich clusters. Considering a mean Pu content of about 30% in the Pu-rich agglomerates, the Am/(U+Pu+Am) ratio is found to be lower than ≈ 2%. Only a few Raman spectra of $U_{1-x}Am_xO_{2\pm\delta}$ have been reported in the literature [71–73]. We will not detail them here as the acquisition conditions of the spectra are not equivalent from one source to another. Nevertheless, the characteristics of the spectra are known to evolve strongly with the Am content. Summarizing the main trends, (i) an upshift and a strong broadening of the T_{2g} mode; (ii) a progressive upshift of the U* region; (iii) strong continuous changes in the relative intensities of the different lines are observed with the increase in the Am content. In particular, the upshift of the T_{2g} mode most probably translates the decrease of the lattice parameter of the fluorite structure with the increase of the Am content. One additional difficulty for using $U_{1-x}Am_xO_{2\pm\delta}$ for comparison is the systematic charge compensation mechanism, U^{5+}-Am^{3+}, observed in those samples. To date, the effects of the

ACCEPTED MANUSCRIPT
Journal of Applied Physics
AIP Publishing
This is the author's peer reviewed, accepted manuscript. However, the online version of record will be different from this version once it has been copyedited and typeset.
PLEASE CITE THIS ARTICLE AS DOI: 10.1063/5.0103348

substitution of Pu by Am are not completely known. Nevertheless, it can be anticipated that such a substitution will lead to differences in the U-O, Pu-O and Am-O bond lengths, as well as some changes in the oxidation degrees of the cations, that will induce distortions in the crystal. One can anticipate that this substitution affects all the characteristics of the Raman spectra. Nevertheless, these effects are expected to be moderate in the concentration range concerned in this work. They cannot call into question the trends observed herein.

5. SUMMARY AND FUTURE DIRECTIONS

A combination of three different techniques, XRD, EPMA and RS (X-Ray diffraction, Electron Probe Micro-analysis and Raman spectroscopy respectively) was implemented to characterize a particular self-irradiated, ^{238}Pu, ^{240}Pu and ^{241}Pu-enriched MIMAS-type MOx fuel sample, which had been stored for 15 years at room temperature under an inert atmosphere, to maximize irradiation effects. For comparison purposes, a specimen from the same batch was submitted to a thermal treatment and was fully analyzed within two months following this treatment. The annealing conditions ensured both a quite complete healing of the defects and to keep the oxygen to metal ratio as close as possible to 2.00. Two of these methods (EPMA and RS) were used in their imaging mode, even if the dimensions that can be analyzed in a reasonable time scale by the two methods are strongly different. In particular, the representativeness of the Raman data can be somewhat discussed.

This particular MIMAS-type MOx fuel sample was highly heterogeneous in nature, more or less composed of three different phases with different Pu contents, and thus different α dose rates. Thus, EPMA was first used to determine the local Pu content, at the µm scale. Then, XRD was implemented to get an order of magnitude of the lattice swelling of the different phases, giving lattice expansions close to the generally accepted value of 0.3%. Finally, RS was used in its imaging mode. From the analysis of the Raman images, it appeared that four different spectral features bring information, namely the T_{2g} mode frequency, its width (and even perhaps asymmetry), the U* intensity and line shape as well as the 2LO intensity, that allow to track the effect of self-irradiation and irradiation damage. Nevertheless, the analysis is somewhat biased due to the specific, strict resonant scattering conditions, that appear to be maximized for U- rich and minimized for Pu-rich agglomerates, respectively using an excitation wavelength at 532 nm. On the other hand, a small softening of the Raman-allowed T_{2g} mode seems to translate the $(U,Pu)O_2$ lattice swelling, while the broadening of this mode most probably track part of the irradiation damage. We are aware that we used rather strong assumptions (defect-free annealed material, possible slight and local deviations from stoichiometry are disregarded) and approximations to use the T_{2g} mode frequency to extract the local Pu content and to track the swelling. Nevertheless, the obtained orders of magnitude fall within the correct expected range. The availability of more samples will undoubtedly make it possible to refine the assumptions used.

ACCEPTED MANUSCRIPT
Journal of Applied Physics
AIP Publishing
This is the author's peer reviewed, accepted manuscript. However, the online version of record will be different from this version once it has been copyedited and typeset.
PLEASE CITE THIS ARTICLE AS DOI: 10.1063/5.0103348

As already observed, the Raman spectrum of $(U,Pu)O_2$ include a defect-induced signature on the high frequency side of the T_{2g} mode, dominated by the Raman-forbidden 1LO mode. Rather subtle differences between the signature of the aged and annealed samples have been obtained, suggesting in particular that the U^1 and U^3 features might track a particular defect environment. Nevertheless, such a specific defect environment cannot be identified on the basis of those measurements alone. Confirmation of these initial trends requires the periodic analysis over time of the same sample after annealing. The isotopic characteristics of this particular sample require that the analyses are to be conducted over a time period of at least three years. In the meantime, a third sample, obtained 18 months after thermal recovery, is being examined using the same protocol described herein. The first trends extracted from the Raman measurements tend to confirm the present observations.

The simplest irradiation damage-induced defects involve interstitials and vacancies. Both defects induce local structural distortions, as well as changes in mass and stiffness constants. These defects are to be charge-balanced. In the simplest case of an oxygen vacancy, this implies a change in the oxidation state of cations in the vicinity of the defect. Such a change of oxidation degree should be evidenced, using X-ray absorption techniques for example, providing the defect content is high enough to be detected. This work is in progress.

Finally, we discussed the trends obtained with two strongly different samples. It is clear that self-irradiation effects are progressive in time. The periodic or sequential analysis of one specific sample over a large time period, at least three years in the present case, must bring more information.

ACKNOWLEDGEMENTS

The authors would like to thank Camille Aloin, Méghan Alibert, Julien Martinez and Guillaume Gabriel for their contributions to the experiments.

The CEA SIFCOE project is greatly acknowledged for its financial support.

AUTHOR DECLERATIONS

Conflict of Interest

The authors have no conflicts to disclose.

DATA AVAILABILITY

The data that support the findings of this study are available from the corresponding author upon reasonable request.

ACCEPTED MANUSCRIPT
Journal of Applied Physics
AIP Publishing
This is the author's peer reviewed, accepted manuscript. However, the online version of record will be different from this version once it has been copyedited and typeset.
PLEASE CITE THIS ARTICLE AS DOI: 10.1063/5.0103348

REFERENCES

[1] S. Grandjean, N. Reyniertronche, A. Salvatores, N. Herlet, X. Heres, C. Poinssot, D. Ode, B. Lorrain, L. Paret, S. Grandjean, N. Reyniertronche, A. Salvatores, N. Herlet, X. Heres, J. Dancausse, C. Poinssot, and L. Paret, 21st Int. Conf. Global 5313 (2015).

[2] J.F. Ziegler, M.D. Ziegler, and J.P. Biersack, Nucl. Instruments Methods Phys. Res. Sect. B Beam Interact. with Mater. Atoms **268**, 1818 (2010).

[3] T. Wiss, O. Dieste-Blanco, A. Tacu, A. Janssen, Z. Talip, J.Y. Colle, P. Martin, and R. Konings, J. Mater. Res. **30**, 1544 (2015).

[4] Y. Ikusawa, K. Morimoto, M. Kato, K. Saito, and M. Uno, Nucl. Technol. **205**, 474 (2019).

[5] C. Duriez, J.P. Alessandri, T. Gervais, and Y. Philipponneau, J. Nucl. Mater. **277**, 143 (2000).

[6] T.D. Chikalla and R.P. Turcotte, Radiat. Eff. **19**, 93 (1973).

[7] W.J. Nellis, Inorg. Nucl. Chem. Lett. **13**, 393 (1977).

[8] M. Noe and J. Fuger, Inorg. Nucl. Chem. Lett. **10**, 7 (1974).

[9] W.C. Mosley, J. Am. Ceram. Soc. **54**, 475 (1971).

[10] C. Hurtgen and J. Fuger, Inorg. Nucl. Chem. Lett. **13**, 179 (1977).

[11] M. Kato, A. Komeno, H. Uno, H. Sugata, N. Nakae, K. Konashi, and M. Kashimura, J. Nucl. Mater. **393**, 134 (2009).

[12] D. Horlait, F. Lebreton, P. Roussel, and T. Delahaye, Inorg. Chem. **52,** 14196 (2013).

[13] E. De Bona, J. Colle, O. Dieste, M. Cologna, G. Baldinozzi, R. Konings, E. De Bona, J. Colle, O. Dieste, M. Cologna, and T. Wiss, MRS Adv. **6**, 213 (2021).

[14] E. De Bona, A. Benedetti, O. Dieste, D. Staicu, T. Wiss, and R.J.M. Konings, Nucl. Inst. Methods Phys. Res. B **468**, 54 (2020).

[15] W.J. Weber, J. Nucl. Mater. **114**, 213 (1983).

[16] W.J. Weber, Radiat. Eff. **83**, 145 (1984).

[17] W.J. Weber, J. Nucl. Mater. **98**, 206 (1981).

[18] L. Van Brutzel, J.M. Delaye, D. Ghaleb, and M. Rarivomanantsoa, Philos. Mag. **83**, 4083 (2003).

[19] H. Balboa, L. Van Brutzel, A. Chartier, and Y. Le Bouar, J. Nucl. Mater. **512**, 440 (2018).

[20] D. Staicu, T. Wiss, V. V. Rondinella, J.P. Hiernaut, R.J.M. Konings, and C. Ronchi, J. Nucl. Mater. **397**, 8 (2010).

[21] O.A. Maslova, G. Guimbretière, M.R. Ammar, L. Desgranges, C. Jégou, A. Canizarès, and P. Simon, Mater. Charact. **129**, 260 (2017).

[22] Z. Talip, S. Peuget, M. Magnin, M. Tribet, C. Valot, R. Vauchy, and C. Jégou, J. Nucl. Mater.

ACCEPTED MANUSCRIPT
Journal of Applied Physics
AIP Publishing
This is the author's peer reviewed, accepted manuscript. However, the online version of record will be different from this version once it has been copyedited and typeset.
PLEASE CITE THIS ARTICLE AS DOI: 10.1063/5.0103348

499, 88 (2018).

[23] Z. Talip, S. Peuget, M. Magnin, L. Berardo, C. Valot, R. Vauchy, and C. Jégou, J. Raman Spectrosc. **48**, 765 (2017).

[24] L. Desgranges, G. Baldinozzi, P. Simon, G. Guimbretière, and A. Canizares, J. Raman Spectrosc. **43**, 455 (2012).

[25] L. Desgranges, G. Baldinozzi, D. Siméone, and H.E. Fischer, Inorg. Chem. **50**, 6146 (2011).

[26] L. Medyk, D. Manara, J.Y. Colle, D. Bouexière, J.F. Vigier, L. Marchetti, P. Simon, and P.H. Martin, J. Nucl. Mater. **541**, 152439 (2020).

[27] A. Massih, *Models for MOX Fuel Behaviour, SKI Report 2006:10* (n.d.).

[28] G. Oudinet, I. Munoz-Viallard, L. Aufore, M.J. Gotta, J.M. Becker, G. Chiarelli, and R. Castelli, J. Nucl. Mater. **375**, 86 (2008).

[29] R. Vauchy, P. Fouquet-Metivier, P.M. Martin, C. Maillard, I. Solinhac, C. Gueneaub, and C. Leoriera, J. Appl. Crystallogr. **54**, 636 (2021).

[30] A. Le Bail, Powder Diffr. **20**, 316 (2005).

[31] P. Thompson, D.E. Cox, and J.B. Hastings, J. Appl. Crystallogr. **20**, 79 (1987).

[32] J. Pouchou and F. Pichoir, J. Phys. **45**, C2 (1984).

[33] G. Leinders, T. Cardinaels, K. Binnemans, and M. Verwerft, J. Nucl. Mater. **459**, 135 (2015).

[34] R. Vauchy, A.C. Robisson, R.C. Belin, P.M. Martin, A.C. Scheinost, and F. Hodaj, J. Nucl. Mater. **465**, 349 (2015).

[35] J.M. Elorrieta, D. Manara, L.J. Bonales, J.F. Vigier, O. Dieste, M. Naji, R.C. Belin, V.G. Baonza, R.J.M. Konings, and J. Cobos, J. Nucl. Mater. **495**, 484 (2017).

[36] T. Livneh and E. Sterer, Phys. Rev. B - Condens. Matter Mater. Phys. **73**, 1 (2006).

[37] T. Livneh, Phys. Rev. B **105**, 1 (2022).

[38] M.A. Pimenta, G. Dresselhaus, M.S. Dresselhaus, L.G. Cançado, A. Jorio, and R. Saito, Phys. Chem. Chem. Phys. **9**, 1276 (2007).

[39] R. Böhler, M.J. Welland, D. Prieur, P. Cakir, T. Vitova, T. Pruessmann, I. Pidchenko, C. Hennig, C. Guéneau, R.J.M. Konings, and D. Manara, **448**, 330 (2014).

[40] M. Kato and K. Konashi, J. Nucl. Mater. **385**, 117 (2009).

[41] Y. Yun, D. Legut, and P.M. Oppeneer, J. Nucl. Mater. **426**, 109 (2012).

[42] J.W.L. Pang, A. Chernatynskiy, B.C. Larson, W.J.L. Buyers, D.L. Abernathy, K.J. McClellan, and S.R. Phillpot, Phys. Rev. B - Condens. Matter Mater. Phys. **89**, 1 (2014).

[43] G. Dolling, R.A. Cowley, and A.D.B. Woods, Can. J. Phys. **43**, 1397 (1965).

[44] H. Li, P. Zhang, G. Li, J. Lu, Q. Wu, and Y. Gu, J. Alloys Compd. **682**, 132 (2016).

[45] L. Medyk, Thesis: L'enjeu de La Maîtrise Des Propriétés Locales (Stœchiométrie, Répartition Cationique…) Lors de La Fabrication Des Combustibles (U,Pu)O_{2-x}: Potentialités

ACCEPTED MANUSCRIPT
Journal of Applied Physics
AIP Publishing
This is the author's peer reviewed, accepted manuscript. However, the online version of record will be different from this version once it has been copyedited and typeset.
PLEASE CITE THIS ARTICLE AS DOI: 10.1063/5.0103348

de La Microscopie Raman, 2021.

[46] M. Naji, N. Magnani, L.J. Bonales, S. Mastromarino, J.Y. Colle, J. Cobos, and D. Manara, Phys. Rev. B **95**, 1 (2017).

[47] R.M. Harker and C. Puxley, Conf. Plutonium Futures, Baden-Baden, Germany, 62 (2016).

[48] E. Villa-Aleman, A.L. Houk, T.C. Shehee, and N.J. Bridges, J. Nucl. Mater. **551**, 152969 (2021).

[49] C. Jégou, R. Caraballo, S. Peuget, D. Roudil, L. Desgranges, and M. Magnin, J. Nucl. Mater. **405**, 235 (2010).

[50] T.R. Griffiths, H.V.S.A. Hubbard, G.C. Allen, and P.A. Tempest, J. Nucl. Mater. **151**, 313 (1988).

[51] T.R. Griffiths and H.V.S.A. Hubbard, J. Nucl. Mater. **185**, 243 (1991).

[52] J. Schoenes, Phys. Rep. **63**, 301 (1980).

[53] P. Ruello, K.D. Becker, K. Ullrich, L. Desgranges, C. Petot, and G. Petot-Ervas, J. Nucl. Mater. **328**, 46 (2004).

[54] T. Mark McCleskey, E. Bauer, Q. Jia, A.K. Burrell, B.L. Scott, S.D. Conradson, A. Mueller, L. Roy, X. Wen, G.E. Scuseria, and R.L. Martin, J. Appl. Phys. **113**, 1 (2013).

[55] G. Grimwall, *Thermophysical Properties of Materials* (1999).

[56] R. Schmitt, A. Nenning, O. Kraynis, R. Korobko, I.A. Frenkel, I. Lubomirsky, M.S. Haile, and L.M.J. Rupp, Chem. Soc. Rev. **49,** 554 (2020).

[57] G. Guimbretière, A. Canizarès, N. Raimboux, J. Joseph, P. Desgardin, L. Desgranges, C. Jegou, and P. Simon, J. Raman Spectrosc. **46**, 418 (2015).

[58] J.M. Elorrieta, L.J. Bonales, V.G. Baonza, and J. Cobos, J. Nucl. Mater. **503**, 191 (2018).

[59] H. Richter, Z.P. Wang, and L. Ley, Solid State Commun. **39**, 625 (1981).

[60] I.H. Campbell and P.. Fauchet, Solid State Commun. **58**, 739 (1986).

[61] J.E. Spanier, R.D. Robinson, F. Zhang, S.W. Chan, and I.P. Herman, Phys. Rev. B - Condens. Matter Mater. Phys. **64**, 1 (2001).

[62] M. Yu, P.Y., Cardona, *Fundamentals of Semiconductors: Physics and Materials* (2010).

[63] M. Cardona, *Light Scattering in Solids II, Chapter 2 Resonance Phenomena* (Springer, 1982).

[64] Y.Q. An, A.J. Taylor, S.D. Conradson, S.A. Trugman, T. Durakiewicz, and G. Rodriguez, Phys. Rev. Lett. **106**, 5 (2011).

[65] K. Rickert, T.A. Prusnick, M.M. Kimani, E.A. Moore, C.A. Merriman, and J.M. Mann, J. Nucl. Mater. **514**, 1 (2019).

[66] C. Schilling, A. Hofmann, C. Hess, and M.V. Ganduglia-Pirovano, J. Phys. Chem. C **121**, 20834 (2017).

ACCEPTED MANUSCRIPT
Journal of Applied Physics
AIP Publishing
This is the author's peer reviewed, accepted manuscript. However, the online version of record will be different from this version once it has been copyedited and typeset.
PLEASE CITE THIS ARTICLE AS DOI: 10.1063/5.0103348

[67] L. Desgranges, A. Canizares, and P. Simon, J. Nucl. Mater. **559**, 153405 (2022).

[68] E. Villa-Aleman, N.J. Bridges, T.C. Shehee, and A.L. Houk, J. Nucl. Mater. **515**, 140 (2019).

[69] J.M. Elorrieta, L.J. Bonales, N. Rodríguez-Villagra, V.G. Baonza, and J. Cobos, Phys. Chem. Chem. Phys. **18**, 28209 (2016).

[70] L.M. Malard, M.A. Pimenta, G. Dresselhaus, and M.S. Dresselhaus, Phys. Rep. **473**, 51 (2009).

[71] M. Naji, J.Y. Colle, O. Beneš, M. Sierig, J. Rautio, P. Lajarge, and D. Manara, J. Raman Spectrosc. **46**, 750 (2015).

[72] F. Lebreton, D. Horlait, R. Caraballo, P.M. Martin, A.C. Scheinost, A. Rossberg, C. Jégou, and T. Delahaye, Inorg. Chem. **54**, 9749 (2015).

[73] E. Epifano, M. Naji, D. Manara, A.C. Scheinost, C. Hennig, J. Lechelle, C. Guéneau, D. Prieur, T. Vitova, K. Dardenne, J. Rothe, P.M. Martin, and R.J.M. Konings, Commun. Chem. **2**, 1 (2019).

Journal of Applied Physics

ACCEPTED MANUSCRIPT

This is the author's peer reviewed, accepted manuscript. However, the online version of record will be different from this version once it has been copyedited and typeset.

PLEASE CITE THIS ARTICLE AS DOI: 10.1063/5.0103348

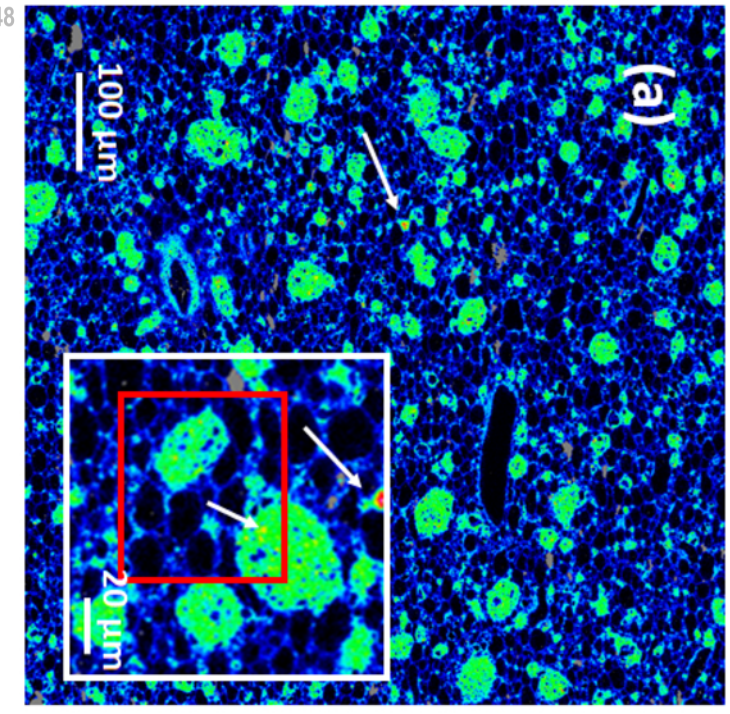

AIP Publishing

Journal of Applied Physics

ACCEPTED MANUSCRIPT

This is the author's peer reviewed, accepted manuscript. However, the online version of record will be different from this version once it has been copyedited and typeset.
PLEASE CITE THIS ARTICLE AS DOI: 10.1063/5.0103348

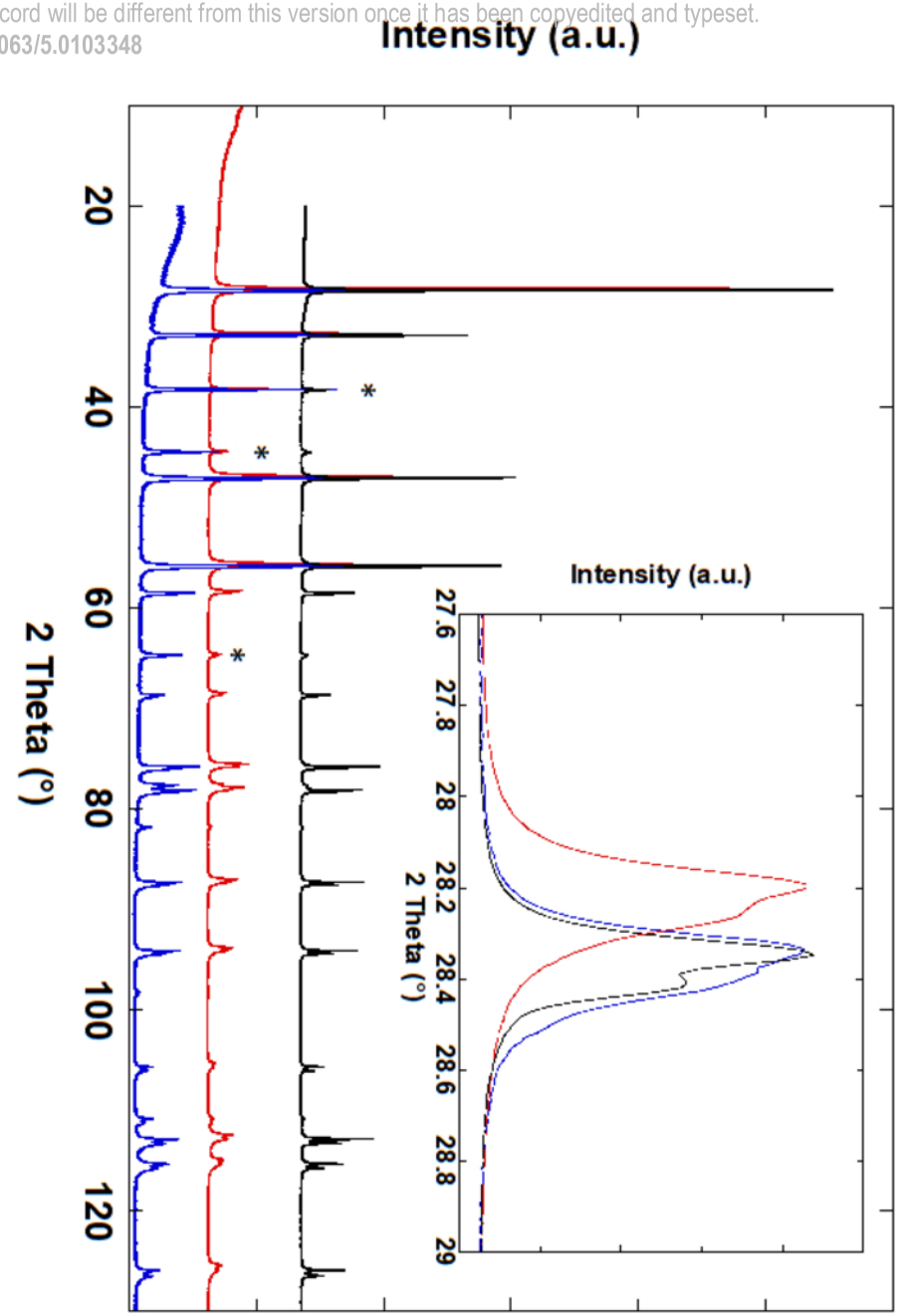

AIP Publishing

Journal of Applied Physics

ACCEPTED MANUSCRIPT

This is the author's peer reviewed, accepted manuscript. However, the online version of record will be different from this version once it has been copyedited and typeset.
PLEASE CITE THIS ARTICLE AS DOI: 10.1063/5.0103348

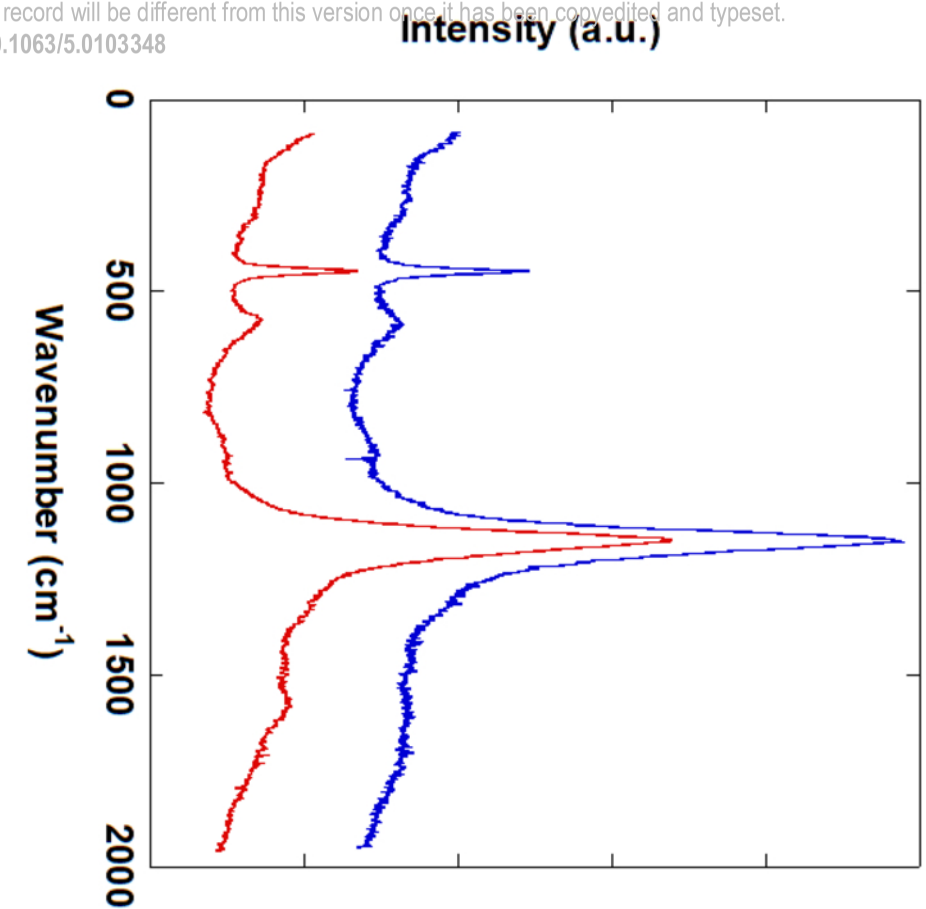

AIP Publishing

Journal of Applied Physics

ACCEPTED MANUSCRIPT

This is the author's peer reviewed, accepted manuscript. However, the online version of record will be different from this version once it has been copyedited and typeset.

PLEASE CITE THIS ARTICLE AS DOI: 10.1063/5.0103348

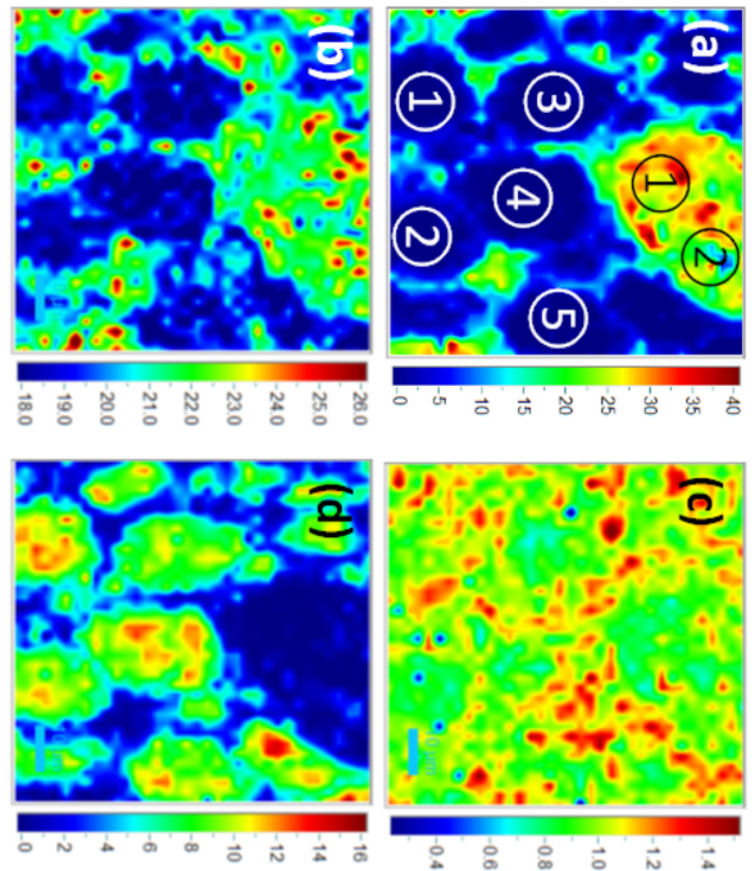

AIP Publishing

Journal of Applied Physics

ACCEPTED MANUSCRIPT

This is the author's peer reviewed, accepted manuscript. However, the online version of record will be different from this version once it has been copyedited and typeset.

PLEASE CITE THIS ARTICLE AS DOI: 10.1063/5.0103348

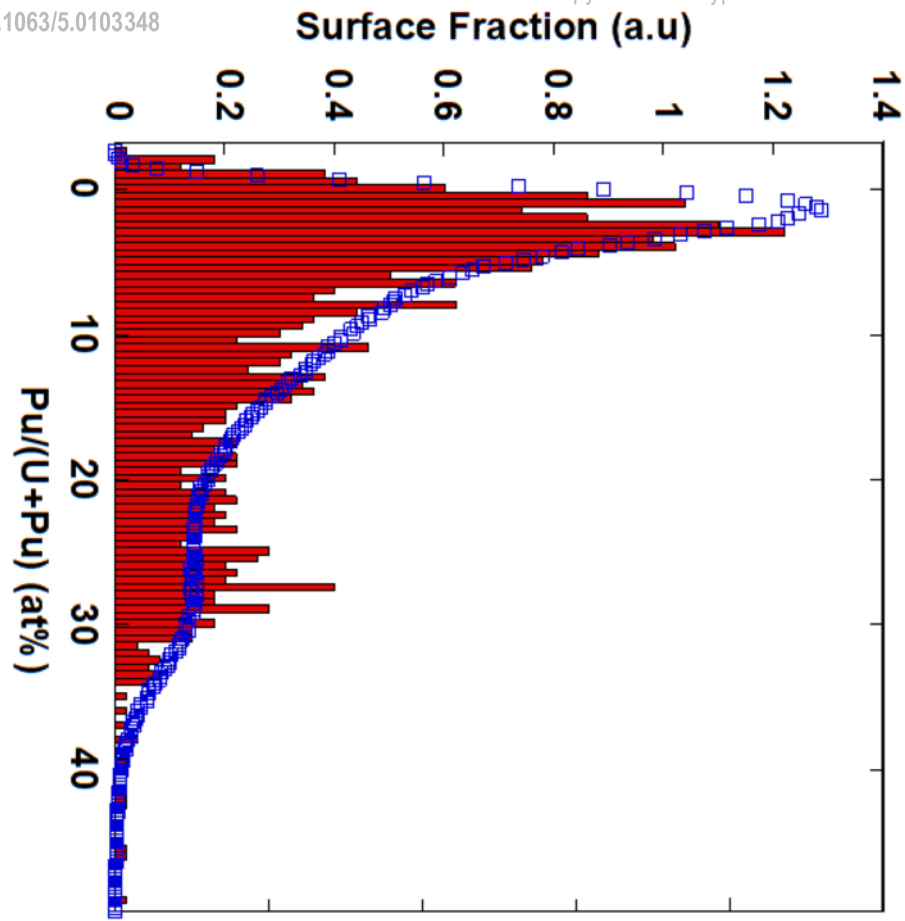

AIP Publishing

Journal of Applied Physics

ACCEPTED MANUSCRIPT

This is the author's peer reviewed, accepted manuscript. However, the online version of record will be different from this version once it has been copyedited and typeset.

PLEASE CITE THIS ARTICLE AS DOI: 10.1063/5.0103348

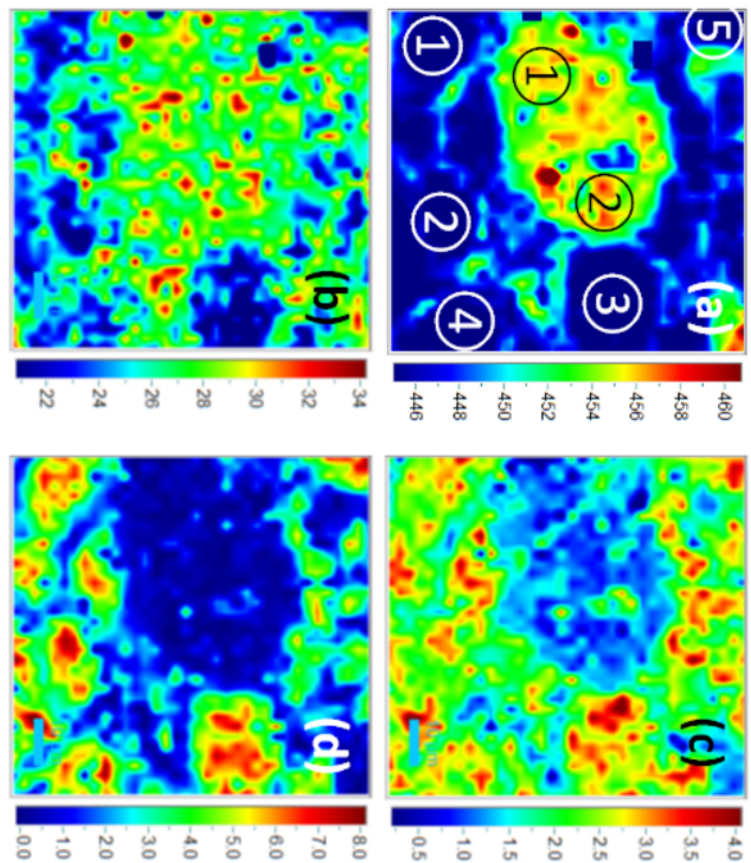

ACCEPTED MANUSCRIPT

Journal of Applied Physics

AIP Publishing

This is the author's peer reviewed, accepted manuscript. However, the online version of record will be different from this version once it has been copyedited and typeset.
PLEASE CITE THIS ARTICLE AS DOI: 10.1063/5.0103348

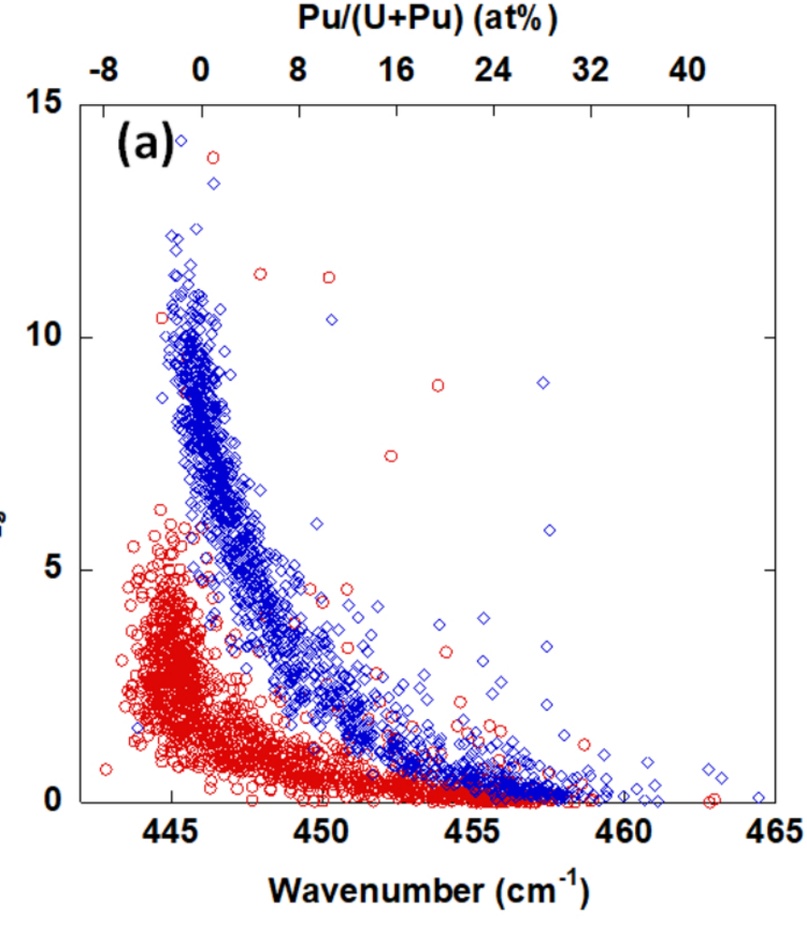

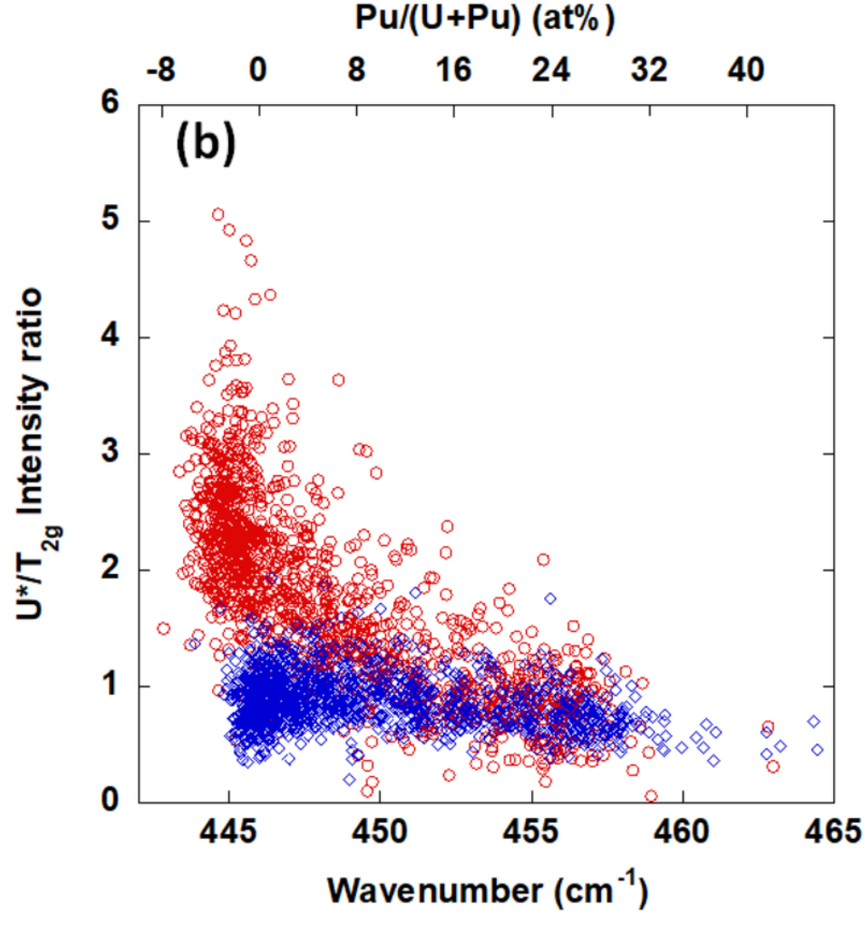

AIP Publishing

Journal of Applied Physics

ACCEPTED MANUSCRIPT

This is the author's peer reviewed, accepted manuscript. However, the online version of record will be different from this version once it has been copyedited and typeset.
PLEASE CITE THIS ARTICLE AS DOI: 10.1063/5.0103348

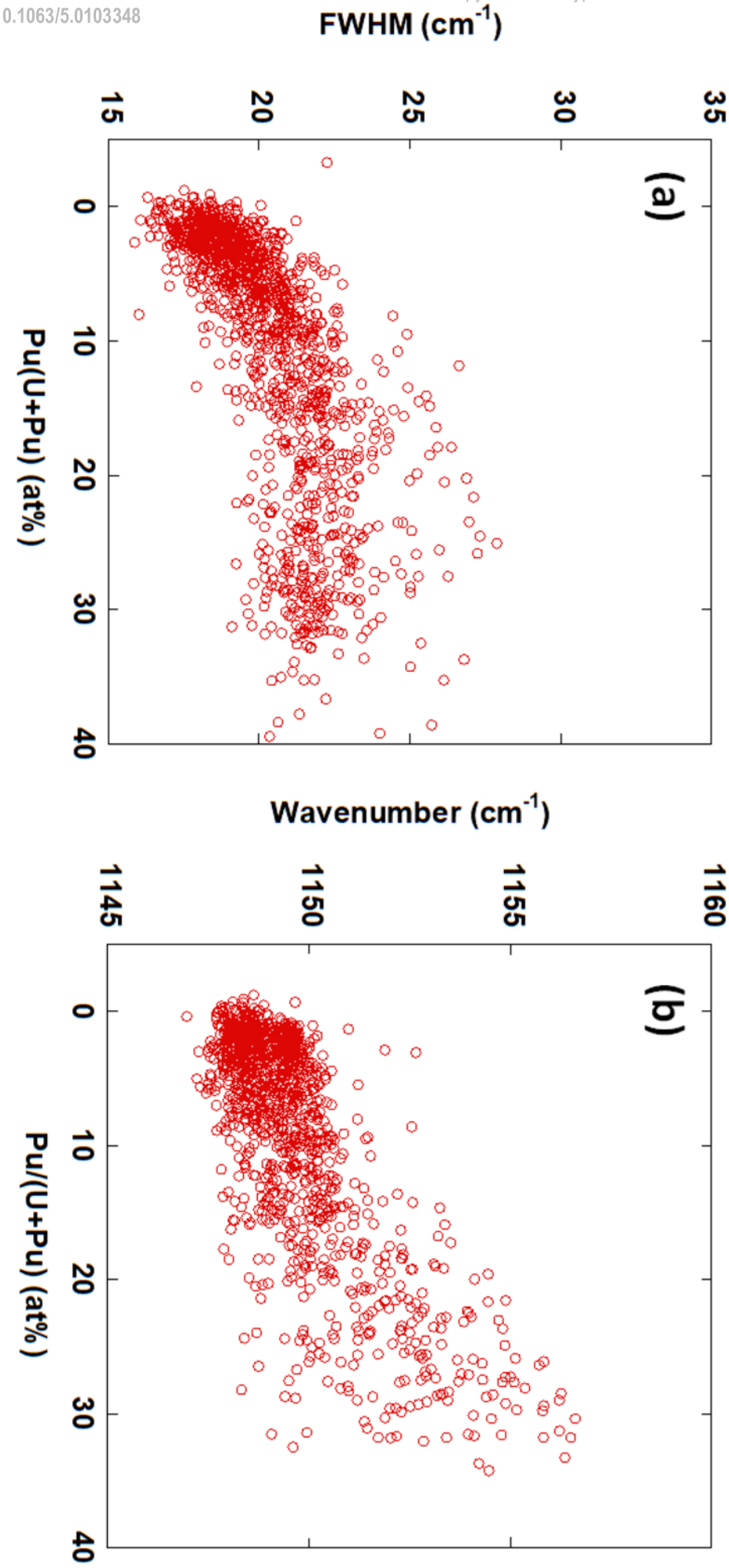

AIP Publishing

Journal of Applied Physics

ACCEPTED MANUSCRIPT

This is the author's peer reviewed, accepted manuscript. However, the online version of record will be different from this version once it has been copyedited and typeset.

PLEASE CITE THIS ARTICLE AS DOI: 10.1063/5.0103348

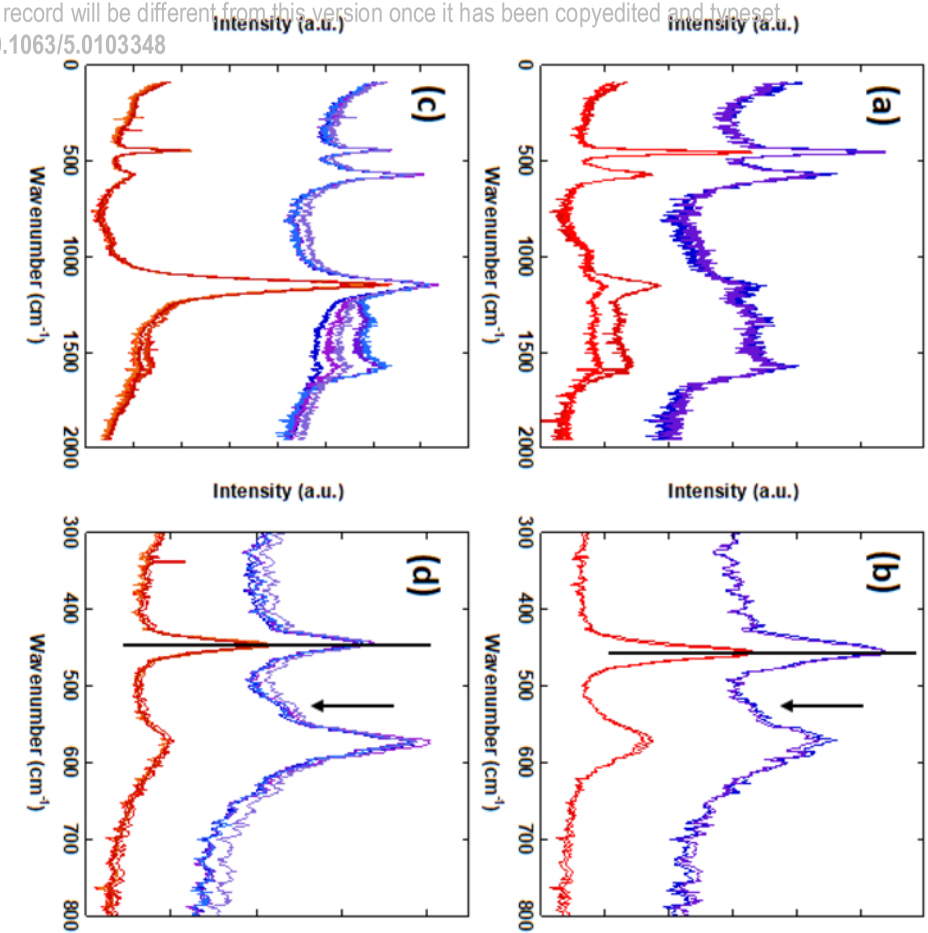

AIP Publishing

Journal of Applied Physics

ACCEPTED MANUSCRIPT

This is the author's peer reviewed, accepted manuscript. However, the online version of record will be different from this version once it has been copyedited and typeset.

PLEASE CITE THIS ARTICLE AS DOI: 10.1063/5.0103348